

Titre: Shimming Toolbox: An Open-Source Software Package for Shimming the B0 and B1 Field in Magnetic Resonance Imaging
Title:

Auteur: Alexandre D'Astous
Author:

Date: 2022

Type: Mémoire ou thèse / Dissertation or Thesis

Référence: D'Astous, A. (2022). Shimming Toolbox: An Open-Source Software Package for Shimming the B0 and B1 Field in Magnetic Resonance Imaging [Mémoire de maîtrise, Polytechnique Montréal]. PolyPublie.
Citation: <https://publications.polymtl.ca/10463/>

 **Document en libre accès dans PolyPublie**
Open Access document in PolyPublie

URL de PolyPublie: <https://publications.polymtl.ca/10463/>
PolyPublie URL:

Directeurs de recherche: Julien Cohen-Adad, & Eva Alonso Ortiz
Advisors:

Programme: Génie biomédical
Program:

POLYTECHNIQUE MONTRÉAL

affiliée à l'Université de Montréal

**Shimming Toolbox: An open-source software package for shimming the B0
and B1 field in Magnetic Resonance Imaging**

ALEXANDRE D'ASTOUS

Institut de génie biomédical

Mémoire présenté en vue de l'obtention du diplôme de *Maîtrise ès sciences appliquées*

Génie biomédical

Août 2022

POLYTECHNIQUE MONTRÉAL

affiliée à l'Université de Montréal

Ce mémoire intitulé :

Shimming Toolbox: An open-source software package for shimming the B0 and B1 field in Magnetic Resonance Imaging

présenté par **Alexandre D'ASTOUS**

en vue de l'obtention du diplôme de *Maîtrise ès sciences appliquées*

a été dûment accepté par le jury d'examen constitué de :

Frédéric SIROIS, président

Julien COHEN-ADAD, membre et directeur de recherche

Eva ALONSO-ORTIZ, membre et codirectrice de recherche

David RUDKO, membre externe

ACKNOWLEDGEMENTS

I would like to specially thank my director, Julien Cohen-Adad, who allowed me to make this project and introduced me to academic research. Julien has played a big role in this project through valuable insights and critical thinking in a favorable learning environment. I would also like to thank my co-director, Eva Alonso-Ortiz, who also provided great feedback, knowledge and suggestions.

I would also like to thank all the fellow members of Neuropoly, but especially Gaspard Cereza who I spent most of my time with at the lab bouncing back ideas. A special thanks to Ryan Topfer whose work and feedback was of great importance. Ryan first tackled the idea of a *Shimming Toolbox* project and explored many of the avenues implemented in this work.

I want to also acknowledge Daniel Papp, Jason Stockman and Nibardo Lopez-Rios specifically for their support and the many people who have contributed to the *Shimming Toolbox* project.

I would like to thank my parents. I would not be the person I am today without them; they have always supported me in whatever goals I had set and this academic endeavour is one of them.

And lastly, I would like to thank my partner Charlotte, who has been with me through the highs, lows and through the long hours while working on this project. She has been striving for me to push myself and made many sacrifices along this journey. I am grateful to have her in my life and for all her support.

RÉSUMÉ

En augmentant le champ magnétique principal (ou champs B_0) en imagerie par résonance magnétique, les images peuvent bénéficier d'une meilleure résolution et d'une meilleure intensité de signal. Cependant, augmenter le champ B_0 comporte plusieurs obstacles, l'un d'entre eux est l'augmentation des inhomogénéités de ce champ. Ces inhomogénéités sont la source de plusieurs effets indésirables comme la perte de signal, la distorsion géométrique, et la superposition de signal dans les images résultantes. Pour mitiger ces artéfacts, un processus appelé B_0 « shimming » est effectué pour homogénéiser le champ. Typiquement, cela consiste à acquérir une carte du champ B_0 et d'utiliser des antennes qui produisent des champs opposés aux inhomogénéités. Plusieurs techniques ont été proposées pour « shim » le champ B_0 comme le « shim » statique (où les coefficients sont optimisés pour un seul volume), le « shim » dynamique (où les coefficients sont optimisés pour chaque tranche d'une image) et le « shim » en temps-réel (où les coefficients sont calculés en temps réel pour corriger les inhomogénéités statiques et ceux qui varient dans le temps). Ces techniques peuvent utiliser plusieurs sortes d'antennes comme celles intégrées dans l'IRM ou des antennes sur mesure.

Un autre obstacle rencontré lorsque le champ B_0 augmente est la diminution de la longueur d'onde de l'onde RF. À 7 Tesla, la longueur d'onde est de l'ordre de grandeur de la tête d'un humain adulte. Cette courte longueur d'onde entraîne des inhomogénéités dans le profil d'excitation, appelé inhomogénéités B_1+ . Ces inhomogénéités créent des effets indésirables tel que la perte locale de signal et des intensités de signaux locaux variables. Pour limiter ces inhomogénéités, des techniques comme le « shimming » statique B_1+ (les courants RF sont calculés pour obtenir un profil d'excitation homogène) ont été développées.

Toutes ces méthodes sont répandues à travers plusieurs groupes de recherches. Elles sont difficiles à reproduire et à implémenter. Elles ont aussi besoin de programmes dédiés et de connaissances importantes pour leur implémentation. Dans ce contexte, le but de ce projet de recherche est de développer un logiciel complet libre d'accès (*Shimming Toolbox*) pour prototyper des techniques de « shimming », tester des antennes, reproduire des techniques de « shimming » existantes, et développer de nouvelles avenues de recherches reliées au « shimming » du champ B_0 . Le « shimming » B_1 a aussi été implémenté dans *Shimming Toolbox* dans le cadre du projet de maîtrise de Gaspard Cereza.

Shimming Toolbox inclut des outils de conversion d'image, de cartographie de champ B0, de création manuelle et automatique de masque, de caractérisation de champ d'antenne et inclut les techniques de « shimming » B0 globale, dynamique et de temps réel ainsi que de « shimming » B1+ statique. Le logiciel est disponible pour téléchargement sur la plateforme Github avec des instructions d'installations, des tutoriels, et de la documentation disponible sur le site internet de *Shimming Toolbox* (<https://shimming-toolbox.org>).

Le logiciel a été testé in-vivo à l'aide de deux expériences qui ont testé l'habileté de faire du « shimming » B0 dynamique et en temps réel en utilisant des antennes intégrées et des antennes sur mesure. Ces expériences ont été effectuées à différent champ (3 T et 7 T) sur différentes parties de l'anatomie (cerveau et moelle épinière). Le « shimming » dynamique a démontré une réduction des inhomogénéités du champs B0 dans le cerveau de 47% et le « shimming » en temps réel a démontré une réduction des inhomogénéités du champs dans la moelle de 30%.

Des recherches futures peuvent se concentrer sur le développement de *Shimming Toolbox* pour pouvoir être plus versatile dans ses choix d'optimiseur, de techniques de cartographie, d'« unwrap » et de techniques de « shimming ». Le logiciel pourrait aussi être optimisé pour être plus rapide afin d'utiliser moins de temps lors des expériences. Même si *Shimming Toolbox* a réduit les inhomogénéités du champ B0, plus de tests sont nécessaires afin de bien évaluer la performance des différentes techniques implémentées. J'espère que *Shimming Toobox* sera une plateforme sur laquelle la communauté IRM va collaborer, utiliser des techniques de « shimming » à l'état de l'art, et rendra la recherche en « shimming » plus transparente et reproductible.

ABSTRACT

By increasing the main magnetic field (or B0 field) in magnetic resonance imaging, images can benefit from better resolution and signal strength. However, increasing the B0 field comes with challenges, one of which is the increased inhomogeneity of that field. Inhomogeneities of the B0 field are the source of multiple undesirable effects such as signal loss, geometric distortions and signal overlap in the resulting images. To mitigate these artifacts, a process called B0 shimming is performed that aims at homogenizing the B0 field. It typically consists of acquiring a map of the B0 field and the use of coils that produce fields which will counteract the inhomogeneities. Multiple techniques have been proposed to shim the B0 field such as static shimming (coefficients are optimized for a single volume), dynamic shimming (coefficients are optimized for each slice) and real-time shimming (coefficients are calculated in real-time to correct both static and time-varying inhomogeneities). These techniques can use the included scanner shim coils or external custom shim coils.

Another challenge encountered when the B0 magnetic field is increased is that the RF wavelength decreases. At 7 Tesla, the wavelength is on the order of the adult human head which results in an inhomogeneous excitation profile, also called B1+ inhomogeneities. These inhomogeneities create undesirable effects such as local loss of signal and intensity variations. To address these issues, techniques such as static B1+ shimming (RF currents are calculated to obtain a homogeneous excitation profiles) have been developed.

All these shimming methods are scattered between research groups, are hard to reproduce, are hard to implement, require dedicated software, and require knowledge to implement. In this context, the goal of this research project is to develop an open-source, end-to-end software package (*Shimming Toolbox*) for prototyping shimming techniques, testing coils, reproducing shimming experiments and develop new research avenues related to B0 shimming. B1 shimming was also implemented in *Shimming Toolbox* as part of Gaspard Cereza's Master thesis.

Shimming Toolbox includes tools for image conversion, B0 field mapping, manual and automatic masking, coil characterisation and performing static, dynamic and real-time B0 shimming as well as static B1+ shimming. The toolbox is available for download on Github with installation instructions, tutorials and documentation available on the *Shimming Toolbox's* website (<https://shimming-toolbox.org>).

The software package was tested in-vivo in two different experiments that tested its ability to perform dynamic and real-time B0 shimming using scanner and custom shim. These experiments were performed at different field strength (3 T and 7 T) and on different part of the anatomy (brain and spinal cord). Dynamic shimming showed a reduction of 47% of B0 field inhomogeneities in the brain and real-time dynamic showed a reduction of 30% of B0 field inhomogeneity in the spinal cord.

Future research could focus on developing *Shimming Toolbox* to be more versatile in its choice of optimizer, field mapping technique, unwrapper and shimming technique. The toolbox could be optimized for speed to save valuable time at the scanner. Although *Shimming Toolbox* reduced B0 inhomogeneities, further testing of the tools is required to appropriately evaluate their performance. It is my hope that *Shimming Toolbox* will provide a platform on which the MRI community can collaborate, use state-of-the-art shimming techniques and make shimming research more transparent and reproducible.

TABLE OF CONTENTS

ACKNOWLEDGEMENTS	III
RÉSUMÉ	IV
ABSTRACT.....	VI
TABLE OF CONTENTS.....	VIII
LIST OF TABLES	XI
LIST OF FIGURES	XII
LIST OF SYMBOLS AND ABBREVIATIONS	XV
CHAPTER 1 INTRODUCTION	1
1.1 Thesis organisation	2
CHAPTER 2 LITERATURE REVIEW	3
2.1 MRI physics	3
2.1.1 Main magnetic field	3
2.1.2 Nuclear spin	4
2.1.3 Magnetisation.....	5
2.1.4 Excitation	6
2.1.5 Relaxation	6
2.1.6 Signal reception	8
2.1.7 Slice selection	8
2.1.8 K-space	9
2.1.9 Sequences.....	11
2.1.10 Other magnetic resonance techniques.....	14
2.2 B0 inhomogeneities	14
2.2.1 Magnetic susceptibility	14
2.2.2 Susceptibility artefacts	15
2.3 B0 shimming.....	15
2.3.1 Field mapping	16
2.3.2 B0 shim coils.....	18
2.3.3 B0 shimming techniques.....	22
2.4 Existing B0 shimming software.....	23
2.4.1 B0 DETOX	23

2.4.2	Harmonized.....	23
CHAPTER 3	PROJECT RATIONALE.....	24
3.1	Main objective	24
3.2	Specific objectives	24
CHAPTER 4	ARTICLE 1: SHIMMING TOOLBOX: AN OPEN-SOURCE SOFTWARE TOOLBOX FOR B0 AND B1 SHIMMING IN MAGNETIC RESONANCE IMAGING	26
4.1	Article introduction.....	27
4.2	Abstract	27
4.3	Introduction.....	28
4.3.1	B0 shimming.....	28
4.3.2	B1+ shimming.....	29
4.3.3	Objectives	30
4.4	Methods.....	30
4.4.1	Overview of <i>Shimming Toolbox</i>	30
4.4.2	Imaging experiments.....	40
4.5	Results.....	44
4.5.1	Scenario 1: B0 dynamic shimming using an AC/DC coil at 7 T.....	44
4.5.2	Scenario 2: Breathing-induced B0 real-time dynamic shimming at 3 T	47
4.5.3	Scenario 3: B1 static shimming at 7 T	49
4.6	Discussion	50
4.6.1	Validation experiments	50
4.6.2	Modularity.....	50
4.6.3	Graphical User Interface (GUI) and scripts	51
4.6.4	Perspective	51
4.6.5	Open-source software development.....	52
4.7	Conclusion	52
4.8	Acknowledgements.....	53
CHAPTER 5	GENERAL DISCUSSION	54
5.1	Develop <i>Shimming Toolbox</i>	54
5.2	Develop a graphical user interface.....	54
5.3	Develop a website	55

5.4	Demonstrate <i>Shimming Toolbox</i> 's B0 shimming feasibility in different scenarios <i>in-vivo</i>	55
5.5	B1+ shimming.....	56
5.6	Limitations	56
CHAPTER 6	CONCLUSION AND RECOMMENDATIONS	58
REFERENCES	59

LIST OF TABLES

Table 2.1: B0 field strength and its relative Larmor frequency in water.	5
---	---

LIST OF FIGURES

Figure 2.1: MRI scanner showing the x-, y- and z- axes.	4
Figure 2.2: Nuclear dipole precessing around the direction of the B ₀ field.	5
Figure 2.3: Net magnetization shown after a 90 degrees excitation pulse. Left: Longitudinal relaxation (<i>T</i> ₁). Center: Transverse relaxation (<i>T</i> ₂). Right: <i>T</i> ₁ and <i>T</i> ₂ relaxation with spin precession.	7
Figure 2.4: Example of k-space being filled by an EPI sequence.	9
Figure 2.5: Pulse sequence diagram showing the RF pulse, gradient pulses and acquisition window. An analog to digital converter (ADC) is used to digitize the acquired signal. Adapted from course GBM8378 at Polytechnique Montreal [24].	10
Figure 2.6: Gradient echo pulse sequence diagram. Adapted from course GBM8378 at Polytechnique Montreal [24].	12
Figure 2.7: K-space trajectory for a GRE.	12
Figure 2.8: Pulse sequence diagram of an echo planar imaging sequence. Adapted from course GBM8378 at Polytechnique Montreal [24].	13
Figure 2.9: Three images of the lower brain to the upper torso are shown from a GRE field mapping sequence. A) Magnitude image. B) Phase difference image with phase wraps. C) Phase difference image unwrapped with Prelude. The image scaling is not the same for all images.	18
Figure 2.10: Spherical harmonic field distribution depending on the order. Courtesy of Allen D. Elster, MRIquestions.com [36].	19
Figure 2.11: Shim and RF transceiver coils. The 24-channel shim coil (left), with 8-channel transceiver atop it (center), inserts into the patient bed table in close proximity to the subject's spine. From [39].	20
Figure 2.12: Top and bottom halves of coil before and after conversion to a combined RF-shim array. From [12].	21
Figure 4.1: Overview of <i>Shimming Toolbox</i> . The toolbox is installed on a computer and can be connected directly to the scanner console to access the images as they are reconstructed. <i>Shimming Toolbox</i> can calculate field maps, define masks and create shim coil calibration profiles, optimize B ₀ and B ₁ shim currents and send the currents to the MRI scanner in predefined format. The bottom right panel illustrates a respiratory-modulated real-time	

- shimming scenario, wherein the shim current for each coil element is dependent on a pressure probe that relates to the patient's respiratory trace. The coefficients are then sent to the scanner or to the custom coil drivers. 31
- Figure 4.2: **A)** Manual creation of a mask using FSLeys' existing interface. **B)** Creation of a brain mask using FSL BET. **C)** Creation of a spinal cord mask using SCT..... 33
- Figure 4.3: Overview of B0 static and dynamic shimming. **Step 1:** The mask is either considered as a single block (static) or multiple slice groups (dynamic), and resampled to the ΔB_0 field map space. **Step 2:** The ROI of the field map is extracted using the mask. **Step 3:** The coil profiles are resampled to the field map space and shimming coefficients are calculated based on the selected solver and criteria. **Step 4:** The coefficients are written to a text file. 35
- Figure 4.4: Real-time dynamic xyz-shimming sequence showing one line of k-space. Gradients (in red) along x, y and z are played out during the pulse sequence to correct for through slice and in-plane homogeneities. The amplitude of these gradients is modulated in real-time by the respiratory pressure trace. Note that the pressure reading was purposely made faster for illustration purpose (one TR is much faster than one breathing cycle). 37
- Figure 4.5: Example text files output by *Shimming Toolbox*. **A)** Text file to be read by the pulse sequence during real-time dynamic shimming. Each block of three rows corresponds to a slice and within that block, a static coefficient, real-time coefficient and mean pressure is provided. **B)** Text file to be read by an Arduino Teensy board in the case of custom shim coils during dynamic shimming [52]. Each row corresponds to a slice and each column a coil channel. **C)** Text file with B1+ shimming coefficients where each row is a transmit channel and the columns are the magnitude and phase coefficients..... 39
- Figure 4.6: Comparison of field maps between the global 2nd order spherical harmonics on the whole brain, the predicted dynamic shim using the AC/DC custom coil and the acquired dynamic shim image with that coil. Standard deviation is shown for each slice in Hz. Slices numbers: A: 16, B: 24, C: 32, D: 40. 44
- Figure 4.7: Comparison of the standard deviation of the B0 field in the brain at 7T for each slice of acquired B0 field maps between global 2nd order spherical harmonics shimming, predicted dynamic shimming and acquired dynamic shimming using an AC/DC coil. 45
- Figure 4.8: Comparison of the distortion between 2nd order SH global shimming and dynamic shimming using a 31-channel custom multi-coil shim array. Column 1 shows a reference

MPRAGE acquisition where the brain outline was segmented for reference using BET and overlaid in red. Columns 2 through 5 show EPI acquisitions with the same acquisition parameters except for the shimming procedure and phase encoding direction. Columns 2 and 3 show global shimming using 2nd order spherical harmonics in the AP and PA phase encoding direction respectively. Column 4 and 5 show dynamic shimming using *Shimming Toolbox* and the multi-coil shim array with phase encoding direction of AP and PA respectively. Slices numbers: A: 16, B: 24, C: 32, D: 40. 46

Figure 4.9: Violin plot comparing the signal distribution within the spinal cord with 2nd order global shimming (black) and with real-time dynamic xyz-shimming (red) for multiple echo times. Mean signal intensity across slices and echo times: global/real-time: 151.54/174.99. Average standard deviation within slices: global/real-time: 19.61/13.81. An axial slice showing the location of the shim ROI for real-time shimming as well as the segmented spinal cord is shown at the bottom left of the plot. 47

Figure 4.10: Comparison between 2nd order global shimming and real-time dynamic xyz-shimming in the spinal cord at 3 T. **(Left)** Localizer showing where the slices are located. **(Center and Right)** Slice number 1 and 2 of the same multi-echo GRE sequence acquired using 2nd order global shimming and real-time dynamic xyz-shimming. 48

Figure 4.11: UNI **(A, B)** and GRE-INV2 images **(C, D)** spinal cord images from the MP2RAGE sequence, normalized by the maximum intensity in the spinal cord. Spinal cords were automatically segmented with SCT (and manually adjusted when required) on CP mode and shimmed images and a co-registration was performed. After shimming, the coefficient of variation in the spinal cord is reduced by 10.59% on UNI images **(A, B)** and 39.72% on GRE images **(C, D)**. 49

Figure 5.1: *Shimming Toolbox*'s GUI is shown with its different processing pipelines (Dicoms to NIfTI, B0 field mapping, masking, B0 shimming and B1+ shimming) represented as tabs. In this tab, B0 dynamic shimming inputs and options can be seen. 55

LIST OF SYMBOLS AND ABBREVIATIONS

A	Anterior
AC	Alternative current
ADC	Analog to digital converter
B0	Longitudinal magnetic field
B1	Radiofrequency electromagnetic field
B1+	Transmit radiofrequency electromagnetic field
BET	Brain extraction tool
BIDS	Brain imaging data structure
BW	Bandwidth
CNR	Contrast to noise ratio
CP	Circularly polarized
DICOM	Digital imaging and communications in medicine
DC	Direct current
EPI	Echo planar imaging
FA	Flip angle
FID	Free induction decay
FMRI	Functional magnetic resonance imaging
FOV	Field of view
GRE	Gradient echo
GUI	Graphical user interface
IRB	Institutional review board
JSON	JavaScript Object Notation
MAE	Mean absolute error

MR	Magnetic resonance
MRI	Magnetic resonance imaging
MSD	Mean standard deviation
MSE	Mean standard error
NIfTI	Neuroimaging Informatics Technology Initiative
NMR	Nuclear magnetic resonance
P	Posterior
RF	Radio frequency
RMSE	root mean squared error
ROI	Region of interest
Rx	Reception
SAR	Specific absorption rate
SCT	Spinal cord toolbox
SH	Spherical harmonics
SMS	Simultaneous multi-slice
SNR	Signal to noise ratio
STD	Standard deviation
T	Tesla
T1	Longitudinal relaxation time
T2	Transverse relaxation time
T2*	Effective transverse relaxation time
TE	Echo time
TR	Repetition time
TTL	Transistor-transistor logic

Tx	Transmission
UNI	Uniform T1 weighted image

CHAPTER 1 INTRODUCTION

Magnetic Resonance Imaging (MRI) is one of the most popular imaging techniques for imaging soft tissues. It provides a safe and non-invasive look inside the human body. Different contrasts and techniques make MRI versatile, allowing it to be one of the best diagnostic tools for clinicians. Researchers and magnetic resonance (MR) manufacturers have always been trying to improve scanners to achieve better images and enhance its diagnostic capabilities. Better resolution and image quality can be achieved by increasing the signal to noise ratio (SNR) and contrast to noise ratio (CNR). A scanner gets its main source of signal through the main magnetic field, called B₀. By increasing this field, the resulting signal also increases which in turn yields better SNR and CNR. Current scanners' B₀ field usually operate at around 1.5 to 3 Tesla (T) but researchers and manufacturers are working on 7 T and higher field strength scanners to acquire better images. However, increasing the B₀ field comes with many challenges, one of which is the inhomogeneity of that field [1]. B₀ inhomogeneities can cause loss of signal, blurring artefacts and geometric distortions that reduce the quality of the images [2]–[4].

A procedure called B₀ shimming [5] aims at homogenising that field. Many techniques have been developed in the past to shim the B₀ field. Such techniques include static shimming, dynamic shimming [6]–[9] and real-time shimming [4], [10]. The development of custom shim coils [11], [12] has also shown to increase B₀ shimming capabilities. These techniques allow to reduce artifacts and recover otherwise lost signal, especially at higher fields.

Another challenge related to the increase of the B₀ field is the inhomogeneity of the RF field. At 7 T, the RF field wavelength is on the order of the object which results in an inhomogeneous excitation profile. Furthermore, when using multiple transmit elements, the inhomogeneities can create interferences which further increase inhomogeneities [13], [14]. These inhomogeneities can lead to signal loss and intensity variations in the resulting image. To mitigate those issues, the interference pattern can be controlled by updating the amplitude and phase of the transmit elements. This process is called B₁₊ or RF shimming [15]–[17].

1.1 Thesis organisation

Most of the work and research that was done regarding this thesis was focused on B0 shimming. B1+ shimming is briefly explained to describe concepts introduced in the research article of Chapter 4. Section 4.1, which introduces the research article, provides a deeper explanation after the main objective and specific objectives have been introduced. Briefly, B1+ shimming was part of Gaspard Cereza's Master's thesis [18] and contributed to the article in Chapter 4.

This thesis is organised in 6 chapters. Chapter 2 provides a literature review of the MRI B0 shimming field to provide the reader a good understanding of this work and its context. Chapter 3 exposes the rationale of the project, the main objective and sub-objectives. Chapter 4 includes a submitted scientific article which describes the main work of this research project. Chapter 5 includes a general discussion about topics not discussed in the main article followed by a last chapter (Chapter 6) that concludes this thesis.

CHAPTER 2 LITERATURE REVIEW

A review of prior work is performed to situate this work in the context of the current MRI field. The general physics behind MRIs is explained to give the reader a better understanding of the concepts that will be introduced. Examples of B0 inhomogeneities and current shimming solutions are also introduced.

2.1 MRI physics

Nuclear magnetic resonance (NMR) was first measured by Isidor Isaac Rabi in 1938 whom received a Nobel prize for his work in 1944 [19]. In 1971, Raymond Damadian proposed to use NMR signals to differentiate healthy from malignant tissues [20]. Six years later, Damadian created the first whole-body human MRI scanner [21]. Since then, scanners have been improved to produce an imaging technique that is non-ionising, provides good spatial resolution (mm scale), provides high contrast and provides quantitative measures of the underlying tissue (e.g., water %, proton density, T_1 , T_2 , T_2^* and others) [22]. MRI has come a long way since the early days of NMR, however, the same basic technology is still in use today. This section aims at providing a base understanding of MRI physics to ultimately understand B0 inhomogeneities.

2.1.1 Main magnetic field

MRI scanners typically use a powerful superconducting electromagnet to generate the B0 magnetic field. This field is ideally constant through the whole imaging region and constant through time. The B0 field is typically orientated along the z-axis of the scanner, parallel to the scanner bore. Figure 2.1 shows the typical x-, y- and z- MRI axes.

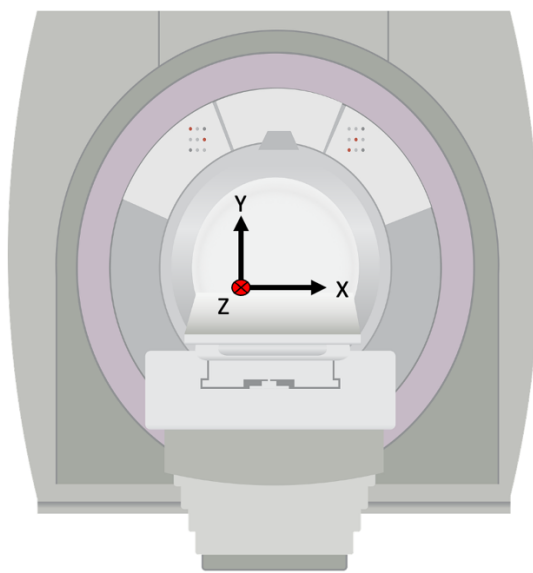


Figure 2.1: MRI scanner showing the x-, y- and z- axes.

2.1.2 Nuclear spin

The nuclei of certain atoms have a property called spin. This property creates a magnetic dipole moment that acts like a tiny magnet (a nuclear magnetic dipole). It emits a weak magnetic field and responds to external fields that are applied in its vicinity. One of those atoms is hydrogen. The abundance of water (H_2O) in the human body, especially in soft tissues, allows the MRI to capture the field emitted from the hydrogen atoms with a coil outside the body.

In the absence of a magnetic field, the nuclear dipoles are orientated in all directions due to thermic noise. When an external magnetic field is applied, the nuclear dipoles align with that field. Due to the intrinsic spin angular momentum property, they also precess around the axis of the applied field which, within the scanner, is aligned with the B_0 field. Figure 2.2 illustrates a nuclear dipole precessing around the direction of the applied B_0 field.

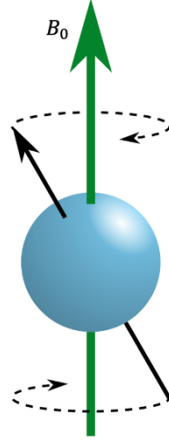


Figure 2.2: Nuclear dipole precessing around the direction of the B_0 field.

The rate at which the dipoles rotate is called the Larmor frequency and is given by:

$$\omega_0 = \gamma B_0 \quad \text{Equation 2.1}$$

$$f_0 = \frac{\omega_0}{2\pi} \quad \text{Equation 2.2}$$

Where ω_0 (*rad*) is the angular frequency at which the dipoles rotate, γ ($\text{rad} \cdot \text{s}^{-1} \cdot \text{T}^{-1}$) is the gyromagnetic ratio, B_0 (T) is the applied magnetic field and f_0 (Hz) is the precession frequency (i.e., Larmor frequency). Since MRI scanners use hydrogen atoms for their signal, the gyromagnetic ratio of hydrogen in water is used. The Larmor frequency for different scanner's B_0 field strength is derived in Table 2.1.

B_0	3 T	7 T
f_0	127.74 MHz	298.06 MHz

Table 2.1: B_0 field strength and its relative Larmor frequency in water.

2.1.3 Magnetisation

When a patient is present in the scanner, the B_0 field aligns the nuclear dipoles along the z-axis. On a larger scale, this results in a net macroscopic magnetization of the dipoles in the body. The magnetization is called the longitudinal magnetisation, which at equilibrium is called M_0 and is given by:

$$M_0 \approx \frac{\rho \gamma^2 \hbar^2}{4kT} B_0 \quad \text{Equation 2.3}$$

Where ρ is the proton density, \hbar is the reduced Planck constant, k is the Boltzmann constant and T is the temperature.

This equation has profound impact on MRI. It says that the magnetization, which is proportional to the resulting acquired NMR signal, is affected by intrinsic properties of the tissue, the temperature, and the B0 field. The temperature can hardly be lowered when imaging patients due to comfort constraints, increasing the B0 field is therefore the only viable option to increase the magnetization. It increases the longitudinal magnetization linearly, directly increasing SNR. With more SNR, it is possible to improve the resolution since less volume is necessary to create the same signal. This is the main reason why manufacturers and researchers are constantly trying to image at higher field strength.

2.1.4 Excitation

To be able to measure a signal, the magnetization's (M) orientation, which is aligned with the B0 field at resting state, needs to be tipped in the transverse plane (x-y). After an excitation pulse, the spins precess around the z-axis with some amplitude in the transverse plane. To tip the spins out of their equilibrium state, they are excited using a radiofrequency (RF) pulse that is transverse to the B0 field at the Larmor frequency. This RF field is called the B1 field. The resulting angle (α) at which the magnetization is deflected from its equilibrium position is described by the flip-angle where t is time and τ is the length of the RF pulse.

$$\alpha = \gamma \int_0^{\tau} B_1(t) dt \quad \text{Equation 2.4}$$

2.1.5 Relaxation

Once the net magnetization is in the transverse plane, it slowly goes back to its original position (aligned with the B0 field) in a process called relaxation. There are two types of relaxation.

Longitudinal relaxation brings back the net magnetization towards the B0 field. It follows an exponential curve with a time constant of T_1 . The following equation describes the signal after time t (assuming $t = 0$ to be when the spins were flipped in the transverse plane) of the component of the net magnetization along the z-axis (M_z):

$$M_z(t) = M_0 \left(1 - (1 - \cos \alpha) e^{-\frac{t}{T_1}} \right) \quad \text{Equation 2.5}$$

Transverse relaxation is due to interactions in the transverse plane. A first effect called spin-spin interactions is due to the random motion of the spins which affect other adjacent spins creating dephasing. This effect follows a different exponential curve with time constant T_2 . A second effect is due to inhomogeneities of the B_0 field, which causes more dephasing in the transverse plane. Both components can be merged into a single effective time constant of T_2^* . The following equation describes the amplitude of the net magnetization in the transverse plane ($|M_{xy}(t)|$) at time t (assuming $t = 0$ to be when the spins were flipped in the transverse plane):

$$|M_{xy}(t)| = M_0 \sin \alpha \left(e^{-\frac{t}{T_2^*}} \right) \quad \text{Equation 2.6}$$

Longitudinal relaxation and transverse relaxation occur at the same time. However, T_2^* decay happens much faster than T_1 , therefore it is possible to omit T_1 relaxation in $M_{xy}(t)$. Flipping the net magnetization in the transverse plane and recording its relaxation is called free induction decay (FID). Figure 2.3 shows both T_1 and T_2 relaxation visually.

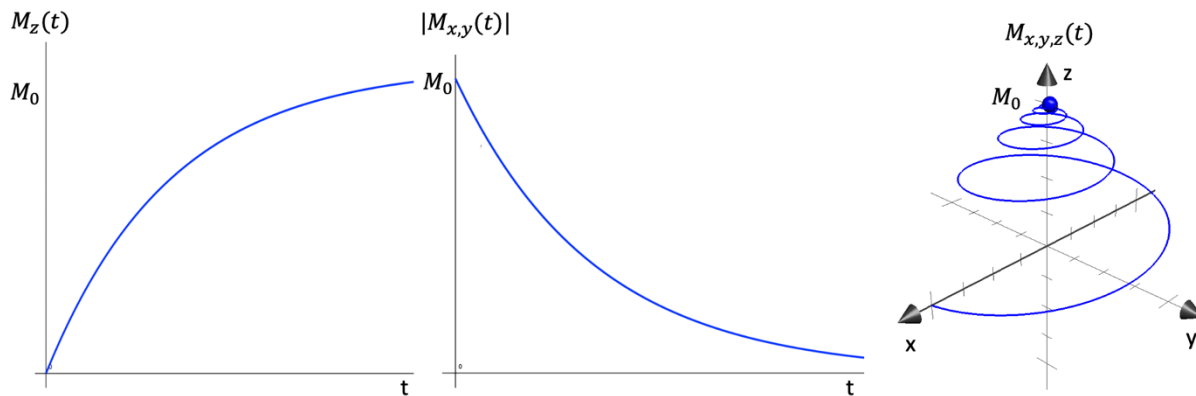


Figure 2.3: Net magnetization shown after a 90 degrees excitation pulse. **Left:** Longitudinal relaxation (T_1). **Center:** Transverse relaxation (T_2). **Right:** T_1 and T_2 relaxation with spin precession.

Both T_1 and T_2 are specific to each tissue and along with proton density ρ , are the main sources of contrast in MRI [23]. Each tissue has its own properties that change those constants which results in a net magnetization amplitude over time that is different depending on the tissue.

2.1.6 Signal reception

The oscillating magnetic field created by the net magnetization in the transverse plane ($M_{xy}(t)$) generates an electrical current in the receiver (Rx) coil. The perceived complex signal ($s(t)$) is proportional to the following equation:

$$s(t) \propto \int M_{xy}(r) e^{-i\phi(r,t)} dr \quad \text{Equation 2.7}$$

Where $\mathbf{r} = x\hat{\mathbf{x}} + y\hat{\mathbf{y}} + z\hat{\mathbf{z}}$, $M_{xy}(r)$ is the net magnetization at a particular point in space and $\phi(r, t)$ is the phase accumulated at time t at a particular point in space.

2.1.7 Slice selection

While it is useful to understand the basic principle of NMR by thinking of a whole body with its spins in unison, it does not provide a particularly good image. To create an image, the spins' frequency is changed to encode spatial locations. To do so, three gradient coils are used. Each gradient coil can generate a magnetic field along the z-axis that varies linearly along x, y, and z respectively (G_x, G_y, G_z). The following equation describes the precession frequency relative to its position \mathbf{r} and the applied gradients.

$$\omega(r) = \gamma B_0 + \mathbf{r} \cdot \gamma \cdot (G_x + G_y + G_z) \quad \text{Equation 2.8}$$

MRI images are acquired in slices. Each slice corresponds to a specific plane of the volume to image. By sequentially changing the imaging plane, a whole volume can be acquired. To select only one slice, a gradient, G_z for perfectly axial slices, is applied. This changes the precession frequency of the spins along the z-axis. At the same time, a B1 RF pulse designed to excite a particular slice thickness is used to flip the selected slice in the transverse plane while not exciting the other spins. Only the signal emitting from that slice will contribute significantly to the net magnetization which will be captured by the reception coils.

2.1.8 K-space

To acquire pixels, the slice must further be divided. To do so, the properties of the Fourier transform are used. K-space is simply a 2D representation of the frequencies in the Fourier domain. By applying a gradient, the relative dephasing along the gradient's direction varies in a sinusoidal pattern. By changing both the x and y gradient, the k-space / Fourier frequencies can be filled using this induced dephasing. When a positive G_x is applied, the location of the acquisition in k-space moves to the right, while a negative G_x moves to the left. Similarly, G_y moves the acquisition up and down.

For example, starting in the middle of k-space, $-G_x$ and $-G_y$ are used to navigate to the bottom left of the k-space, then a continuous G_x is applied while the coil acquires at its sampling frequency (f_s). When reaching the right of k-space, G_x and the Rx coil are stopped. A small G_y is applied to move up, then a continuous $-G_x$ is applied, returning to the left of k-space where a small G_y is used. This is repeated until the top of k-space is reached. Figure 2.4 illustrates the directory in k-space and Figure 2.5 shows the pulse sequence diagram of the example.

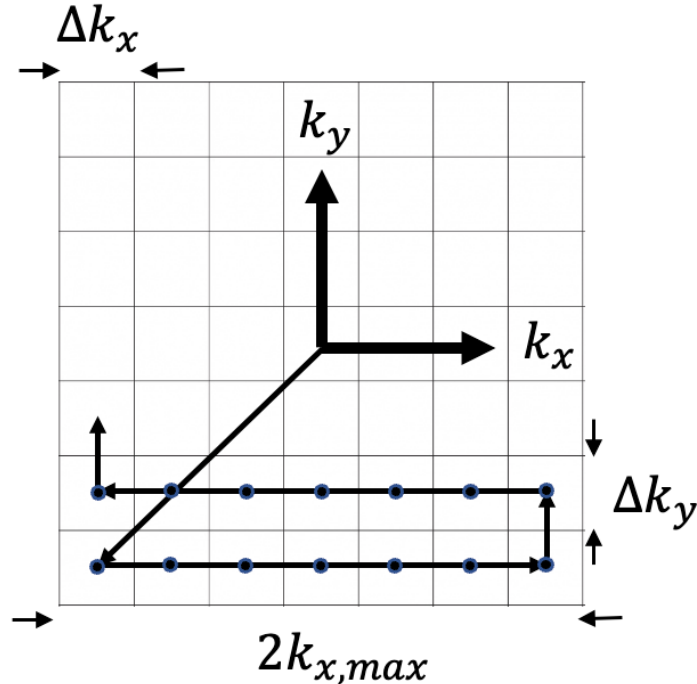


Figure 2.4: Example of k-space being filled by an EPI sequence.

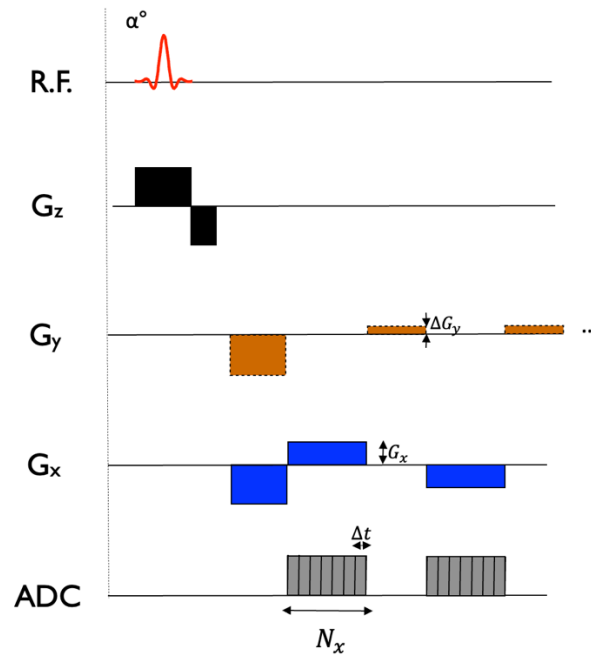


Figure 2.5: Pulse sequence diagram showing the RF pulse, gradient pulses and acquisition window. An analog to digital converter (ADC) is used to digitize the acquired signal. Adapted from course GBM8378 at Polytechnique Montreal [24].

At this point, performing the inverse Fourier transform of k-space yields an image. In practice, the direction in k-space used while the reception coil is active is called the frequency encoding direction (x in this example). The phase encoding direction is the direction orthogonal to both the slice encoding direction and the frequency encoding direction (y in this example).

The number of points acquired in k-space (N_x and N_y), the gradient strengths (G) and the time of application of the gradient (T) can be linked to the extent of k-space ($2k_{x,max}$) using the following equation:

$$2k_{x,max} = N_x \gamma G_x T \quad \text{Equation 2.9}$$

The pixel resolution and the field of view (FOV) can be inferred:

$$\Delta x = \frac{1}{2k_{x,max}} \quad \text{Equation 2.10}$$

$$\Delta y = \frac{1}{2k_{y,max}} \quad \text{Equation 2.11}$$

$$FOV_x = N_x \Delta x \quad \text{Equation 2.12}$$

$$FOV_y = N_y \Delta y \quad \text{Equation 2.13}$$

The previous equations indicate that the more points acquired in k-space, the better the resolution of the resulting image. It also indicates that careful selection of the gradient strength and sampling frequency needs to occur to acquire an image that extends far enough over the imaging region to properly frame the subject.

2.1.9 Sequences

There are multiple ways to fill the k-space, each having their own benefits and inconveniences that can be observed in the resulting images. This work will only touch on gradient echoes (GRE) and on echo planar imaging (EPI), therefore only these two methods are described. Before diving into the sequences, some terminology is useful to introduce.

- The time between two RF pulses is called TR .
- When applying a gradient, the spins are dephased. If the same gradient is applied with negative polarity, the spins return back in phase. This phenomenon is called an echo. The time between a RF pulse and the middle of an echo (time at which the spins come back in phase) is called TE .

2.1.9.1 Gradient echo

A gradient echo sequence uses much of the same principle as described in section 2.1.8. A RF pulse excites the spins of a particular slice, gradients are controlled to navigate one line in the frequency encoding direction. Once that line has been acquired, a spoiler gradient is applied to shuffle the spins. This effectively brings the acquisition back to the middle of k-space and a second line can be acquired with another RF pulse. Figure 2.6 shows an example pulse sequence diagram and Figure 2.7 shows the first 2 acquisition lines in k-space of a gradient echo. While not shown for simplicity, a second echo could be acquired by applying a $-G_x$ after the end of the first echo.

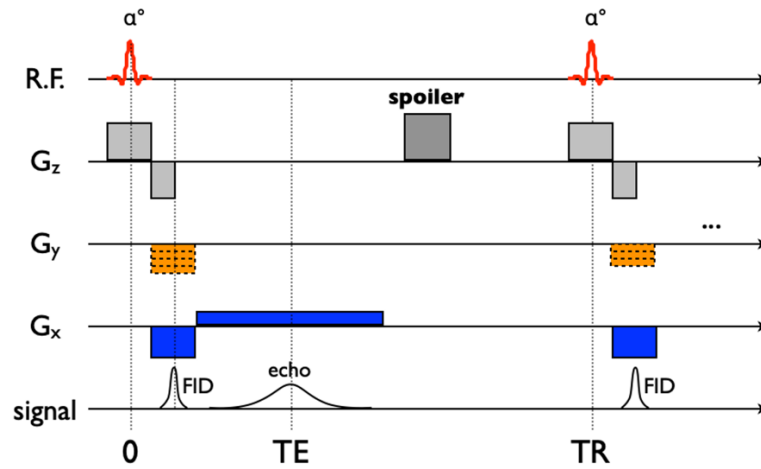


Figure 2.6: Gradient echo pulse sequence diagram. Adapted from course GBM8378 at Polytechnique Montreal [24].

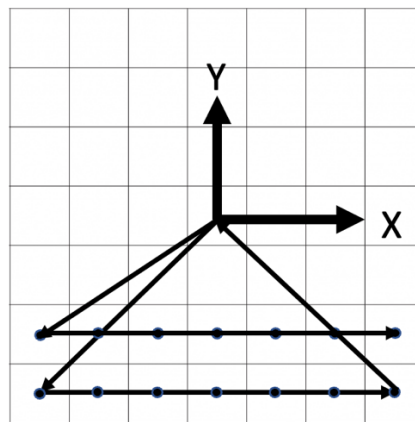


Figure 2.7: K-space trajectory for a GRE.

2.1.9.2 Echo planar imaging

Echo planar imaging sequences are also useful in MRI. They sacrifice signal strength and accuracy for speed. Compared to a GRE sequence, they are much faster and can acquire an entire slice in a single TR. Figure 2.8 shows an example pulse sequence diagram of a single-shot EPI sequence. A RF pulse flips the spins of a slice in the transverse plane and the gradients are then used to navigate k-space very rapidly until the whole k-space is acquired. The process is repeated for each slice. Figure 2.4 shows the first two lines of k-space being filled by this pulse sequence.

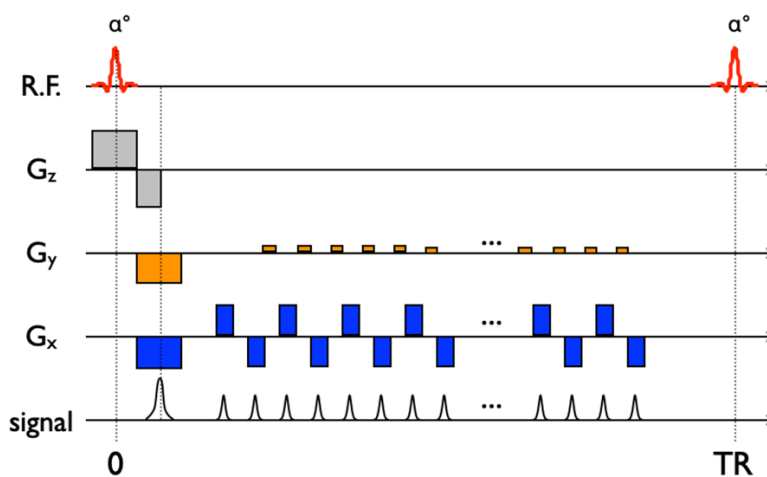


Figure 2.8: Pulse sequence diagram of an echo planar imaging sequence. Adapted from course GBM8378 at Polytechnique Montreal [24].

2.1.10 Other magnetic resonance techniques

2.1.10.1 Simultaneous multi-slice

Simultaneous multi-slice (SMS) is a technique that allows one to acquire different slices at the same time therefore reducing acquisition times [25]. The RF pulse is designed in such a way to excite slices of different locations at the same time. Although the specifics are beyond the scope of this work, the signal can be resolved with the use of multiple receiver channels (parallel imaging) and precise gradient work.

2.2 B0 inhomogeneities

As seen in section 2.1, MRIs rely on the different magnetic fields to encode the spatial location and signal emitted from objects being imaged. These fields are under the assumption that they are “perfect” to produce images that are free from distortions. In practice, this is not the case. One of the main sources of distortion arises from the inhomogeneity of the B0 field. There are two main causes that explain the inhomogeneities of that field: inhomogeneities due to the hardware of the scanner and inhomogeneities due to the patient being scanned [26]. While hardware imperfections are present, they are not the main source of inhomogeneity, especially at higher field strength [27]. Patient induced field variations such as magnetic susceptibility differences, are the main reason for the B0 field inhomogeneity.

2.2.1 Magnetic susceptibility

Magnetic susceptibility (χ) describes the tendency of a material to interact with, and distort an applied magnetic field [28], [29]. It is a lesser-known property of materials since most have very weak susceptibility and therefore have little to no effect on magnetic fields at low strength. However, MRIs operate at very high fields (e.g., 3 T) and even weak susceptibility can have an impact on the magnetic field.

When a patient is introduced in the scanner, the different parts of the body are magnetized by the B0 field and emit back a magnetic field due to their susceptibility. The shape and strength of the emitted field depends on the shape, size, position and susceptibility of the tissue, and is proportional to the applied B0 field [28]. Most notably, irregular tissue shapes and different tissue interfaces that have large susceptibility differences can cause inhomogeneities in the B0 field [28]. This is

often the case for air-tissue interfaces where the susceptibility of human tissue is diamagnetic ($\chi_{water} \approx \chi_{tissue} \approx -9.035 \times 10^{-6}$) and the susceptibility of air is paramagnetic ($\chi_{air} \approx +3.6 \times 10^{-7}$).

2.2.2 Susceptibility artefacts

The magnetic field distortions created by different magnetic susceptibility in the different tissues make spins precess differently than if they were in a perfectly homogeneous field. These effects are more prominent near the sinuses, oral cavities, ears and lungs due to the air-tissue interfaces. These frequency changes induce undesirable effects such as:

- Loss of signal from intravoxel $T2^*$ dephasing (inhomogeneity within a voxel).
- Geometric distortions due to the filling of k-space following a distorted trajectory. This phenomenon is more prominent in EPI [2].
- Warped slice profile due to the slice selection pulse exciting an inhomogeneous field along the slice-axis.
- Disruption of frequency selective RF pulses such as fat saturation pulses [3].
- Ghosting, blurring and ringing artefacts due to phase inconsistencies between RF excitations [4].

Since susceptibility induced field are proportional to the B_0 field, MRI scanners operating at higher field strength are more prone to these artefacts [30].

2.3 B_0 shimming

To limit the effects of these artefacts, it is necessary to homogenize the B_0 field. This process is referred to as B_0 shimming. There are two main ways to do so:

Passive shimming: MRI manufacturers provide a magnet that is not perfectly homogeneous, and environmental factors of the MRI installation site can further increase the inhomogeneities. Passive shimming is the first step to provide a good shim. During installation, small pieces of ferromagnetic objects are introduced in the scanner to get a field that is as homogeneous as possible. This is aimed at correcting hardware induced inhomogeneities. While this technique is a good first step, it does not allow to correct for patient specific inhomogeneities.

Active shimming: Active shimming consists of using specifically designed coils to generate a field that will counter the local inhomogeneities. These coils are called shim coils. The currents running through these coils can be controlled and optimized to produce a field that is as close as possible to the opposite of the B0 field offset ($\Delta B0_{in}$). The field distribution created by each shim coil channel (P_k) is multiplied by the current applied to that channel (I_k). Those field distribution are summed together using the theorem of superposition for all (n) channels. The following equation shows this process and the resulting offset from the B0 field ($\Delta B0_{out}$). An optimization is performed to minimize a criterion in a region of interest (ROI) such as the standard deviation (STD), the mean squared error (MSE) or the mean absolute error (MAE) of $\Delta B0_{out}$.

$$\Delta B0_{out} = \Delta B0_{in} + \sum_{k=0}^n P_k I_k \quad \text{Equation 2. 14}$$

This work will focus on active shimming. The following sections introduce different coils and techniques that have been developed to achieve better active shimming.

2.3.1 Field mapping

The first step to perform shimming is to get an accurate representation of the B0 field. To do so, scanners use sequences that allow to calculate a $\Delta B0$ field map that describes the change from the B0 field. This process is referred to as field mapping.

There are multiple ways to calculate a field map. One way is through a double-echo GRE sequence. By acquiring an image at two different echo times (m_1 at TE_1 and m_2 at TE_2), information about the underlying field can be recovered. More specifically, the difference in phase between the two echoes for a given location can indicate the precession frequency at that point by using the following equation.

$$\Delta\omega(x, y) = \frac{\Delta\phi(x, y)}{TE_2 - TE_1} \quad \text{Equation 2. 15}$$

Where $\Delta\omega(x, y)$ is the angular frequency offset from the B0 field in radians/seconds, which is usually referred to as a $\Delta B0$ field map (or B0 field map). The difference in phase ($\Delta\phi(x, y)$ or phase difference image) can be calculated from the 2 echo images.

$$\Delta\phi(x, y) = \angle m_1^*(x, y)m_2(x, y) \quad \text{Equation 2. 16}$$

Where “ \angle ” is the angle operator and “ $*$ ” is the complex conjugate operator. This is commonly called the complex difference.

2.3.1.1 Unwrapping

Since phase data is defined over 2π , an MRI phase pixel value of 0.5π has the same value as 2.5π . This effect manifests as spatial discontinuities when the phase transitions from $-\pi$ to π . These transition zones are called phase wraps and their number scales with TE . To resolve this effect, spatial unwrapping programs are used like Prelude [31], and others [32]–[34]. This results in an image free of wraps. These algorithms are not perfect, therefore it is usually better to minimize the number of wraps. To do so in dual-echo field mapping, unwrapping is computed on the phase difference image (rather than unwrapping images at each TE) so that the number of wraps scales with the difference in echo time (ΔTE). Since TE_1 and TE_2 are always positive, ΔTE will always be lower or equal to TE_2 as shown by the following equation.

$$\Delta TE = TE_2 - TE_1 \quad \text{Equation 2.17}$$

Figure 2.9 shows a magnitude image for anatomical reference, a phase difference image containing multiple wraps and an unwrapped phase difference image.

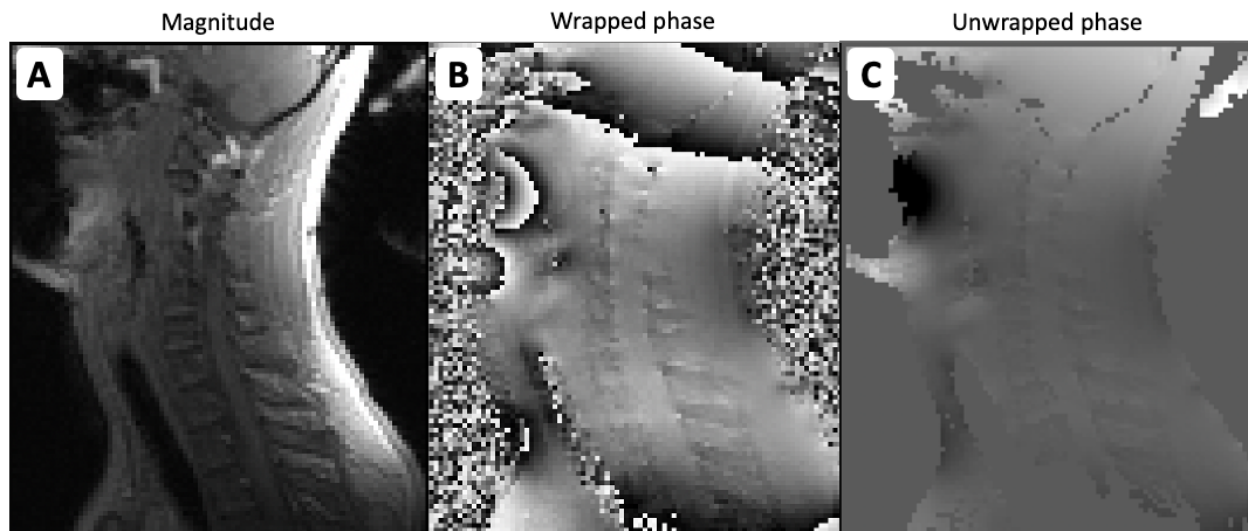


Figure 2.9: Three images of the lower brain to the upper torso are shown from a GRE field mapping sequence. **A)** Magnitude image. **B)** Phase difference image with phase wraps. **C)** Phase difference image unwrapped with Prelude. The image scaling is not the same for all images.

Other field-mapping techniques require to unwrap phase images of different volumes. Some applications include field mapping of more than two echoes as well as acquiring multiple field maps sequentially which can be useful for real-time shimming (see section 2.3.3.3). In those cases, a $2n\pi$ offset (n is an integer) can occur between two independently unwrapped phase volumes due to the unwrapper selecting different regions to be the true B_0 field. To solve this problem, post processing solutions have been proposed that calculate the mean phase over a particular region for both unwrapped volumes and adjust the field by a $2n\pi$ factor if the difference is greater than $n\pi$ [35]. Those solutions assume that the phase offset due to the B_0 field inhomogeneity between the two volumes that are being unwrapped (two echoes or two timepoints) have a phase offset lower than $\pm\pi$.

2.3.2 B_0 shim coils

Shim coils are used by applying currents that generate an opposite field as the measured B_0 field map. There are multiple shim coils available, the following sections describe some of them.

2.3.2.1 Spherical harmonics

The first kind of shim coils are coils that are designed to reproduce the fields of the spherical harmonic (SH) expansion. Any complex magnetic field can be recreated by using the weighted

sum of spherical harmonics terms. The first term is referred to as order 0 and corresponds to a constant value (B_{cst}). Order 1 contains 3 linear terms (x, y and z). The equation below shows how the spherical harmonics can be used to represent the actual field (B_{actual}).

$$B_{actual} = B_{cst} + (B_x + B_y + B_z) + (B_{zx} + B_{zy} + B_{x^2-y^2} + B_{xy} + B_{z^2}) + \dots \text{Equation 2.18}$$

By design, scanners already have order 0 (global B0 offset) and order 1 (x, y and z linear gradients) which explains the use of the spherical harmonics in MRI scanners. MRI manufacturers have also added the 2nd order, and some the 3rd order spherical harmonics but limitations such as space make the availability of higher order limited. These coils can correct for inhomogeneities of simple complexity because of their low spatial variation due to their low SH order. Figure 2.10 shows a visual representation of the spherical harmonics.

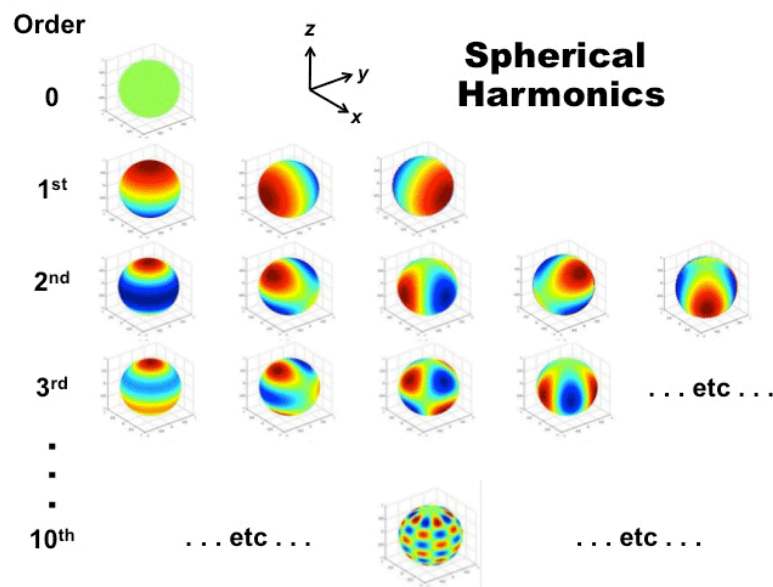


Figure 2.10: Spherical harmonic field distribution depending on the order. Courtesy of Allen D. Elster, MRIquestions.com [36].

2.3.2.2 External shim coils

External shim coil arrays (i.e., multi-coil) are used to supplement the SH coils. They use a combination of multiple localized loops (or channels) typically located close to the imaging region to improve shimming. They have multiple advantages over spherical harmonics coils. Multi-coils have field geometries that would require spherical harmonics of high orders. Since they are localized, they can be specifically made to produce fields that benefit shimming a particular region. They are also more efficient since they are located closer to the imaging region. Their currents can usually be changed more rapidly since they have less inductance due to being smaller. The number of channels can be increased to improve the degrees of freedom while shimming. Multiple groups have designed such arrays [37]–[39] and Figure 2.11 shows one of these coils.

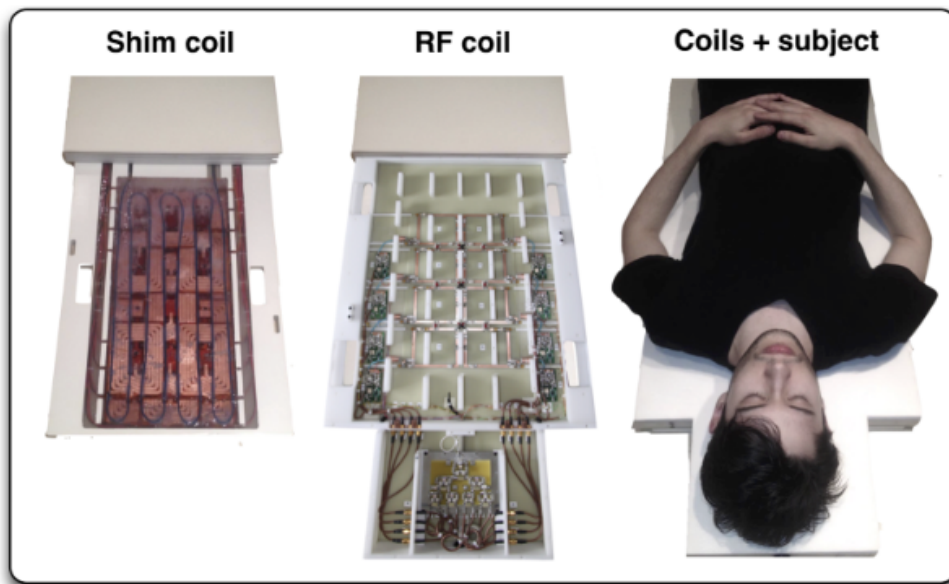


Figure 2.11: Shim and RF transceiver coils. The 24-channel shim coil (**left**), with 8-channel transceiver atop it (**center**), inserts into the patient bed table in close proximity to the subject's spine. From [39].

2.3.2.3 AC/DC coils

While shim coil arrays provide many benefits, they compete for space with the RF coil since both perform better the closer they are to the imaging region. To remedy this problem, hybrid coils that allow RF and B₀ shim currents to circulate through the same loops have been introduced [12], [40]. This is possible since currents of different frequencies can coexist without affecting each other. With clever circuit designs, the direct current (DC) is used to produce a constant field offset that enables B₀ shimming while the alternative current (AC) can still be used as a normal RF coil. Stockmann et al. [12] were able to combine their shim coil with a Rx receiver RF coil shown in Figure 2.12.



Figure 2.12: Top and bottom halves of coil before and after conversion to a combined RF-shim array. From [12].

2.3.3 B0 shimming techniques

B0 shimming is typically performed by acquiring a B0 field map, selecting a ROI, fitting the field geometry of the selected shim coils over that region and calculating the currents that best minimize the B0 offset. There are multiple techniques that have been developed over the years, the following sub-sections describe the most notable.

2.3.3.1 Static shimming

The earliest form of active shimming consists of selecting a ROI and calculating shimming coefficients over the entire region. The coefficients are optimized for a whole volume and stay the same throughout the acquisition. Static (or global) shimming is available on all modern scanners using the spherical harmonics coils up to order 3 (if available). It is possible to use other shim coils as well.

2.3.3.2 Dynamic shimming

Dynamic shimming makes use of the fact that MRI scanners can acquire in slices. Shimming coefficients are specifically calculated for each slice and dynamically updated during the acquisition [6], [7]. The idea behind dynamic shimming is that the smaller the region being shimmed, the more precise the shim can be. Dynamic shimming through spherical harmonics is possible on MRI scanners but limitations often exist due to higher orders (2nd and above) not supporting the rapid switch of currents required due to their high inductance which can induce undesired eddy currents when switching them rapidly [41], [42]. Dynamic xyz-shimming (using the 1st order spherical harmonics) was shown to be possible, reduce geometric distortions and reduce signal dropouts in EPI [8], [43]. Multi-coil arrays and AC/DC coils have also been used by multiple groups and have shown further improvements [44]–[46].

2.3.3.3 Real-time shimming

Real-time shimming tries to account for inhomogeneities that vary through time. Examples of such inhomogeneities are breathing related field induced inhomogeneities. The varying amount of air in the lungs changes the B0 field during the length of an acquisition, which lead to ghosting and blurring [4], [10]. By characterizing this time varying B0 field with the respiratory cycle of an individual, the B0 field can be maintained more constant through the acquisition. Real-time shimming aims at increasing the homogeneity by correcting for both the static component and real-

time component. It can also be combined with dynamic shimming to correct both through time and per slice. Real-time shimming was first demonstrated by Gelderen et al. [4] using the spherical harmonics and later reproduced by Alonso-Ortiz et al. [10]. Both showed reduced ghosting artefacts in GRE sequences.

2.4 Existing B0 shimming software

Some tools are available in the MRI community to use some of the techniques and coils mentioned in section 2.3.

2.4.1 B0 DETOX

B0 DETOX [47] is a software tool which was introduced in 2017, it provides B0 shimming capabilities for static and dynamic shimming using SH and external shim coils. The software is written in MATLAB and requires the MATLAB Runtime Environment to run the code. The software is free of use for non-commercial use in academia and is under a term-limited license.

2.4.2 Harmonized

The “Harmonized” toolbox [48], introduced in 2021, provides B0 shimming solutions for SH coils. The toolbox aims at providing an alternative method to the default shimming algorithm that is proprietary to MRI manufacturers. The software is open-source and written in Julia. Harmonized toolbox is free of use and has been tested on phantoms [48].

CHAPTER 3 PROJECT RATIONALE

The literature review from the previous chapter has allowed to identify the direction to take for this research project. To achieve better image quality and improve resolution, SNR and CNR rely on the increase of the B0 field. Such increase in field strength comes with challenges. One of them is the increase in inhomogeneity of the B0 field, which results in undesirable effects such as loss of signal, geometric distortions, blurring, ghosting and other artefacts. Shimming is necessary for good image quality at high field to reduce these inhomogeneities and limit these artefacts. Multiple techniques have been developed such as static shimming, dynamic shimming and real-time shimming. Shim coils have been developed to further increase the capabilities of these techniques. While MRI scanners can shim using their built-in coils, they do not have the ability to compute shimming solutions for custom shim arrays. Furthermore, not all scanners can compute dynamic coefficients and fewer can compute real-time coefficients using the provided software of the scanner. All these shimming methods are scattered between research groups, are hard to reproduce, are hard to implement and require dedicated software and knowledge.

The MRI community would greatly benefit from an open-source, end-to-end software toolbox for B0 shimming. While there are toolboxes that do provide advanced B0 shimming capabilities [47], [48], there is no free and open source code that:

- Promotes transparent implementation of a variety of shimming algorithms.
- Enables the research community to contribute to it by adding cutting-edge methods.
- Supports static, dynamic and real-time shimming using SH and external shim coils.

3.1 Main objective

The goal of this research project is to develop *Shimming Toolbox*, an end-to-end open-source software package for prototyping shimming techniques, testing coils, reproducing shimming experiments and developing new research avenues related to B0 shimming.

3.2 Specific objectives

The specific objectives that will allow to achieve the main objective of this research project are:

Objective 1: Develop *Shimming Toolbox*, an open-source software toolbox to perform B0 shimming experiments. This includes developing static, dynamic and real-time shimming that have the ability to use custom shim coils and coils that use spherical harmonic.

Objective 2: Develop a graphical user interface (GUI) for interfacing with *Shimming Toolbox*.

Objective 3: Develop a website for providing installation instructions, tutorials on how to use the toolbox and documentation about the code in *Shimming Toolbox*.

Objective 4: Demonstrate the use of *Shimming Toolbox* on human participants.

In the following chapter, a research article where *Shimming Toolbox*'s main features are shown. The toolbox's B0 shimming capabilities are also tested in two experiments in the brain and in the spinal cord with different shimming techniques and coils.

CHAPTER 4 ARTICLE 1: SHIMMING TOOLBOX: AN OPEN-SOURCE SOFTWARE TOOLBOX FOR B0 AND B1 SHIMMING IN MAGNETIC RESONANCE IMAGING

Journal - Submitted to Magnetic Resonance in Medicine – Wiley

June 30, 2022

Alexandre D'Astous¹, Gaspard Cereza¹, Daniel Papp¹, Kyle M. Gilbert², Jason P. Stockmann^{3,4},
Eva Alonso-Ortiz¹, Julien Cohen-Adad^{1,5,6,7}

1: NeuroPoly Lab, Institute of Biomedical Engineering, Polytechnique Montréal, Montréal, QC, Canada

2: Centre for Functional and Metabolic Mapping, The University of Western Ontario, London, Ontario, Canada

3: Athinoula A. Martinos Center for Biomedical Imaging, Massachusetts General Hospital, Charlestown, MA, United States,

4: Harvard Medical School, Boston, MA, United States

5: Functional Neuroimaging Unit, CRIUGM, Université de Montréal, Montréal, QC, Canada

6: Mila - Quebec AI Institute, Montréal, QC, Canada

7: Centre de recherche du CHU Sainte-Justine, Université de Montréal, Montréal, QC, Canada

4.1 Article introduction

The following article introduces the *Shimming Toolbox* to the research community. While the toolbox's original objective is to provide B0 shimming solutions, a portion of the toolbox focuses on B1 shimming; making the RF field that excites the spins as homogeneous as possible, which is another major problem that MRI is facing at higher field strength [49]. B1 shimming was part of the research thesis of Gaspard Cereza [18]. The following article introduces both the B0 and B1 shimming capabilities of *Shimming Toolbox* but it should be noted that the work done in this research thesis involves building the toolbox's software platform from the ground up for B0 shimming and making sure that it was versatile enough so that other shimming solutions could be implemented (e.g., B1 shimming).

4.2 Abstract

Purpose: Introduce *Shimming Toolbox* (<https://shimming-toolbox.org>), an open-source software package for prototyping new methods and performing static, dynamic and real-time B0 shimming as well as B1 shimming experiments.

Methods: *Shimming Toolbox* features various field mapping techniques, manual and automatic masking for the brain and spinal cord, B0 and B1 shimming capabilities accessible through a user-friendly Graphical User Interface (GUI). Validation of *Shimming Toolbox* was demonstrated in three scenarios: (i) B0 dynamic shimming in the brain at 7 T using custom AC/DC coils, (ii) B0 real-time shimming in the spinal cord at 3 T, and (iii) B1 static shimming in the spinal cord at 7 T.

Results: The B0 dynamic shimming of the brain at 7 T took about 10 minutes to perform. It showed a 47% reduction in the standard deviation of the B0 field, associated with noticeable improvements in geometric distortions in EPI images. Real-time dynamic xyz-shimming in the spinal cord took about 5 minutes and showed a 30% reduction in the standard deviation of the signal distribution. B1 static shimming experiments in the spinal cord took about 10 minutes to perform and showed a 40% reduction in the coefficient of variation of the B1 field.

Conclusion: *Shimming Toolbox* provides an open-source platform where researchers can collaborate, prototype and conveniently test B0 and B1 shimming experiments. Future versions will include additional field map preprocessing techniques, optimization algorithms and compatibility across multiple MR manufacturers.

4.3 Introduction

In a quest for better magnetic resonance (MR) images, scanners have gotten ever more powerful by increasing the main source of signal in MR imaging (MRI), the B0 field. A higher B0 field increases signal-to-noise ratio (SNR) and contrast to noise ratio (CNR), allowing one to image at a higher spatial and/or temporal resolution. However, stronger magnets also introduce their own challenges; the increased inhomogeneity of the B0 field when scanning the human body [1] as well as inhomogeneities of the B1 field [49]. These issues, and potential solutions to address them, are described hereafter.

4.3.1 B0 shimming

B0 inhomogeneities lead to artifacts such as geometric distortions in echo planar imaging (EPI) images [2], signal loss from intravoxel T2* dephasing, disruption of frequency selective RF pulses such as fat saturation pulses [3], ghosting [4], signal overlap and others. To reduce these artifacts, it is necessary to homogenize the B0 field, a procedure known as B0 shimming.

Passive shimming, which consists of adding pieces of ferromagnetic objects to change the magnetic field in the scanner, does not allow for the correction of patient specific inhomogeneities. However, active shimming, which consists of updating the currents sent to specialized coils, provides the necessary functionalities to mitigate those inhomogeneities.

Active shimming is typically performed by acquiring a ΔB_0 field map, which describes the offset from the nominal B0 field. This field map is used along with coils and a shimming region of interest (ROI) to calculate the currents (or shim coefficients) that should be used to achieve an optimal B0 field. Different techniques and coils have been developed over the years to improve active B0 shimming.

4.3.1.1 Active shimming techniques

Static (or global) shimming: Optimize shim currents for a specified volumic ROI. These currents stay the same throughout an acquisition. This is the most popular shimming technique.

Dynamic shimming: The shim currents are optimized separately for each slice to be acquired. This technique requires rapid changes of the shim currents over the course of an acquisition, adding

constraints on the shim coils. Dynamic shimming was shown to further improve image quality when compared to static shimming [6], [7].

Real-time shimming: The shim currents are modulated over time to compensate for time-varying B0 field, which could occur with breathing [4], [50].

4.3.1.2 Coils used for shimming

Spherical harmonics: Scanners are equipped with coils that produce fields that follow the spherical harmonic (SH) expansion. Scanners typically have 1st (gradient coils), 2nd and sometimes 3rd order shim coils. Moreover, dynamic shimming is usually restricted to the 1st order due to the high inductance of higher order coils, inducing undesired eddy currents when switching them rapidly [41], [51]. The low order of SH in MRI scanners limit their effectiveness since it can only reduce field offset patterns of low spatial variability.

External shim coils: Shim-only coils can supplement the existing SH-based coil systems of the scanner to provide additional degrees of freedom and shimming performance. These are typically located close to the imaging target and are designed to achieve a desired field geometry and strength [37], [38], [50].

AC/DC coils: These coils combine the functionality of reception (Rx) and/or transmission (Tx), and shimming of the magnetic field in a single coil. A notable advantage of AC/DC coils compared to external shim coils is that they are closer to the region of interest, further improving shimming performance [40], [52].

4.3.2 B1+ shimming

As the field strength increases, the RF wavelength decreases. At 7 T and above, this wavelength becomes of the same order as the image field of view, inducing an inhomogeneous excitation profile known as B1+ inhomogeneities. These inhomogeneities result in a spatially varying flip angle over the image, yielding artifacts/challenges such as variations of tissue contrast, improper inversion pulses, non-optimal fat saturation and excessive specific absorption rate (SAR) [53], [54].

By measuring the B1+ distribution generated by the different transmit elements in the patient's body (procedure known as B1+ mapping), one is able to find a set of optimal shim weights (phase and magnitude of the excitation pulses) that, when applied to the MRI sequence, results in an

improved B1+ homogeneity, and therefore a more uniform image intensity and contrast. This process is commonly referred to as B1+ static (or global) shimming, i.e., the whole volume of interest is shimmed simultaneously and the shim-weights are not modified throughout the sequence. Analogous to B0 shimming, one can also perform B1+ dynamic and real-time shimming, but as those are not yet implemented in *Shimming Toolbox*, we will not consider them further. For the sake of clarity, in the rest of the manuscript we will use the term ‘B1’ when referring to ‘B1+’.

4.3.3 Objectives

To apply and optimize the B0 and B1 shimming techniques reviewed above, a proper software ecosystem is required. While the software console that comes with the MR system can perform basic B0 and B1 shimming, the more advanced techniques are often not available (especially those based on external/custom shim coils). Moreover, shimming algorithms can vary across manufacturers and their implementation is partially opaque (for proprietary reasons), hampering the standardization and transparency of shimming methods. While some freely available toolboxes exist for B0 shimming ([B0 Detox](#) [55], [Harmonized](#) [48]) and B1 shimming ([Parallel Transmission RF Shimming GUI](#) [56], [cardiac_RF_shimming](#) [57]), to the best of our knowledge, there is no open-source all-in-one software that can accommodate a variety of B0 and B1 shimming experiments. Here we introduce *Shimming Toolbox* (<https://shimming-toolbox.org>), an open-source software package for prototyping new methods and performing static, dynamic and real-time B0 as well as RF shimming experiments. We validated *Shimming Toolbox* for B0 shimming on different coils (scanner SH, 31 channel AC/DC array [46]), different field strengths (3 T and 7 T), two different imaging sites, different users and different techniques (dynamic, real-time). We also validated the toolbox for B1 global shimming. Both B0 and B1 shimming experiments were conducted on healthy participants.

4.4 Methods

4.4.1 Overview of *Shimming Toolbox*

Shimming Toolbox is installed on a separate computer running macOS or Linux (Windows support is planned). *Shimming Toolbox* can be used ‘offline’ with already acquired data, or it can be connected to the scanner and process shim coefficients during an imaging session. In the latter

case, the laptop running *Shimming Toolbox* is connected under the same VLAN as the MRI console and a disc is mounted so that images are readily accessible on the laptop for processing.

Shimming Toolbox is written in Python and has been designed to be used on the command line with simple calls to its different functionalities. A Graphical User Interface (GUI) is also available in the form of a plugin to FSLEyes [58] which offers an intuitive way to use the toolbox, look through data, and verify shimming outputs. Figure 4.1 shows an overview of *Shimming Toolbox*. Detailed functionalities are described in the subsequent sections.

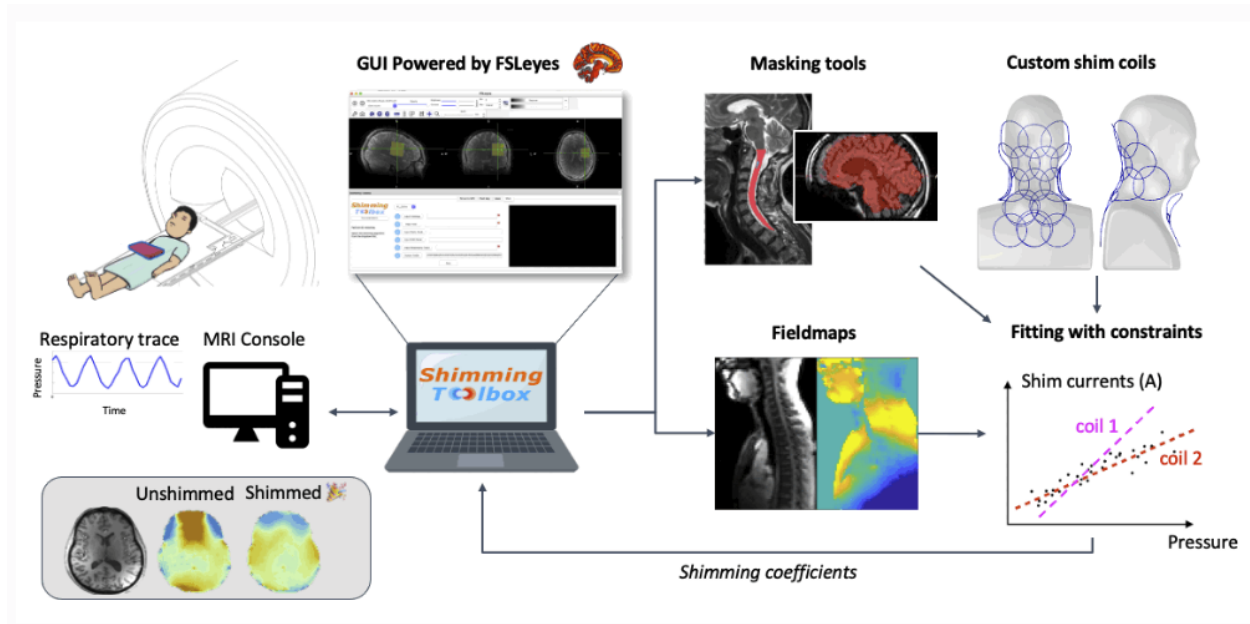


Figure 4.1: Overview of *Shimming Toolbox*. The toolbox is installed on a computer and can be connected directly to the scanner console to access the images as they are reconstructed. *Shimming Toolbox* can calculate field maps, define masks and create shim coil calibration profiles, optimize B0 and B1 shim currents and send the currents to the MRI scanner in predefined format. The bottom right panel illustrates a respiratory-modulated real-time shimming scenario, wherein the shim current for each coil element is dependent on a pressure probe that relates to the patient's respiratory trace. The coefficients are then sent to the scanner or to the custom coil drivers.

4.4.1.1 Convert DICOM to NIfTI files

The first step consists in converting the acquired data into a common format that will be used throughout the different steps of the processing pipeline. We chose the NIfTI format because of its popularity and ease of access to its metadata. DICOM data is converted using `dcm2niix` [59] and subsequently organized into the Brain Imaging Data Structure (BIDS) [60], [61] using `dcm2bids` [62]. Advantages of the BIDS structure is that imaging and field map files are separated into separate folders and their properties, useful for shimming experiments, are well described by a JSON sidecar.

4.4.1.2 Create B0 field maps

Shimming Toolbox supports single NIfTI file phase difference input as well as dual-echo input by computing the complex ratio of the two echoes. We have plans to support more echoes and techniques in the future. Phase images are spatially unwrapped using FSL's *prelude* [31] as an external dependency. Future support for other unwrappers such as UMPIRE [34] and ROMEO [33] is planned. If images do not need unwrapping (e.g.: the sequence already does it), this step can simply be skipped and unwrapped fieldmaps can be input into *Shimming Toolbox*. Field maps acquired through different timepoints (4D) are also supported, allowing for seamless processing of a time series of field maps.

4.4.1.3 Create B0 coil profiles

B0 coil profiles describe the geometry of the z-component of the static magnetic field generated by each shim coil element. *Shimming Toolbox* includes a comprehensive pipeline to generate B0 coil profiles for MRI-system based (i.e.: gradient and shim coils) and custom coils.

To create coil profiles for gradient/shim systems integrated in the MR scanner, we use SH functions to generate the different orders available in the scanner. These are computed at runtime (it takes less than 10 seconds for a $100 \times 100 \times 100$ matrix at spherical harmonic order 2, on a MacBook Pro, M1 Max) to accommodate the different coordinate systems used by different scanner manufacturers.

To create coil profiles for custom shim coils, the user runs a series of ΔB_0 field map scans with different currents for each of their coil channels. These field maps are then processed by linearly fitting field offsets with input currents, coil wise. The output is a NIfTI file containing the coil

profiles for each channel, and a JSON file describing the different constraint parameters of the coils (e.g., maximum current per channel, total current allowed by the amplifiers).

4.4.1.4 Create masks

Masks define the spatial region where B0 or B1 shimming should be optimized. Manual masking is possible via FSLeaves GUI to create different shapes and select specific ROIs. Masks can also be created automatically in the brain using Brain Extraction Tool (BET) [63] or in the spinal cord using the Spinal Cord Toolbox (SCT) [64]. These scenarios are illustrated in Figure 4.2. If the target image on which to apply shimming is of low quality (e.g., gradient echo EPI at coarse resolution), an anatomical image can be acquired and displayed in the FSLeaves GUI for a more accurate masking procedure. If necessary, a co-registration between the target image and the anatomical image can be performed before proceeding with masking.

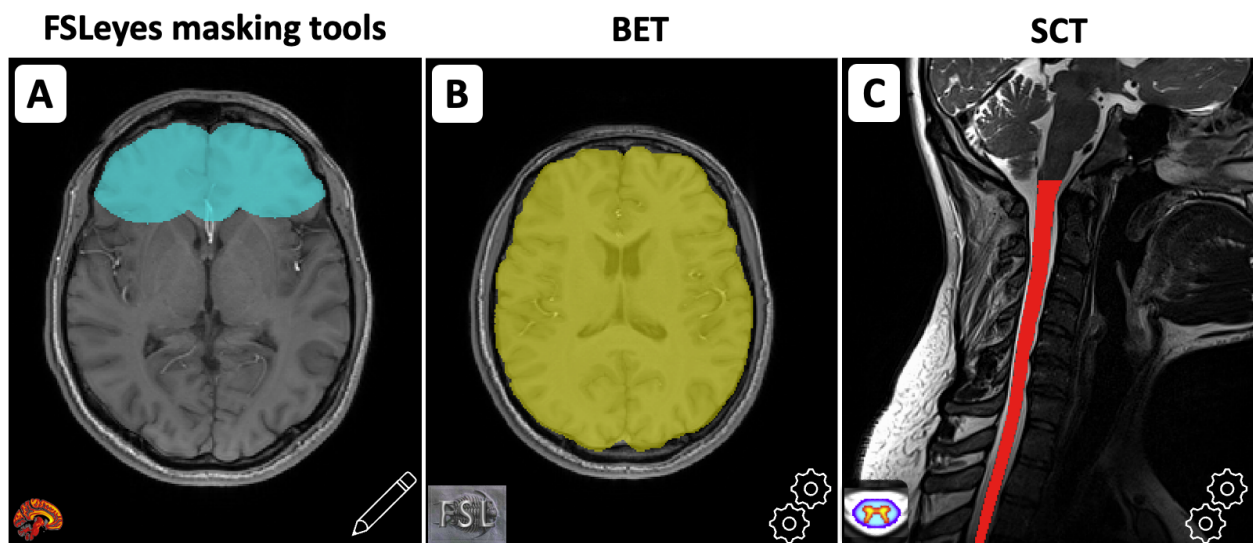


Figure 4.2: **A)** Manual creation of a mask using FSLeaves' existing interface. **B)** Creation of a brain mask using FSL BET. **C)** Creation of a spinal cord mask using SCT.

4.4.1.5 B0 shimming

4.4.1.5.1 Static shimming

The required inputs are: (i) a ΔB_0 field map, (ii) a target image, (iii) a mask, (iv) shim coil profiles and their respective constraints. The target image is acquired with the same sequence as the acquisition that the user wants to shim. It is used to know the image dimensions and the orientation for which shimming will be optimized, as well as useful metadata information about the imaging sequence to be shimmed.

The target image, mask and coil profiles are resampled on the ΔB_0 field map so that the optimization is computed at the resolution of the acquired ΔB_0 field. An optional dilation step on the mask is possible to increase the size of the mask and include more voxels for the optimization.

Shimming Toolbox features a sequential least square programming solver that minimizes a desired criteria, such as the mean squared error (MSE), the mean absolute error (MAE) or the standard deviation (STD) of the ΔB_0 field in the selected ROI . An additional L1 regularization term can be specified to penalize converging solutions that require a high current per channel (or across channels), which is particularly useful in a B0 dynamic shimming scenario (see below) where current rapidly varies across slices. Using the coil-specific constraints, currents can be limited to respect coil limits.

4.4.1.5.2 Dynamic shimming

In dynamic shimming, each slice is submitted to a specific set of shim coefficients. This mode is only available for 2D multi-slice acquisitions. The pipeline is very similar to static shimming. It differs by optimizing each slice separately. The required inputs are: (i) a ΔB_0 field map, (ii) a target image, (iii) a mask, (iv) shim coil profiles and their respective constraints. The slice ordering information is automatically parsed from the target image (via the JSON sidecar) to output the coefficients correctly for ascending, descending, interleaved and simultaneous multi-slice acquisitions. In the latter case of simultaneous multi-slice (also called multiband), shimming will be optimized across the slices that are being simultaneously excited and acquired.

The target image and coil profiles are resampled on the ΔB_0 field map. The mask is then used along with the slice information to create multiple masks containing the ROI for each slice. Each slice of the mask is then individually resampled on the field map. A dilation step is particularly

useful in dynamic shimming if using thin slices, as this adds more pixels for the optimization in the through slice direction.

The same solver (sequential least square programming) and criteria (MSE, MAE, STD) described in the static shimming section are used for dynamic shimming. The ΔB_0 field is optimized for each slice in the ROI, yielding coefficients that will minimize the selected criteria. The pipeline is summarized in Figure 4.3.

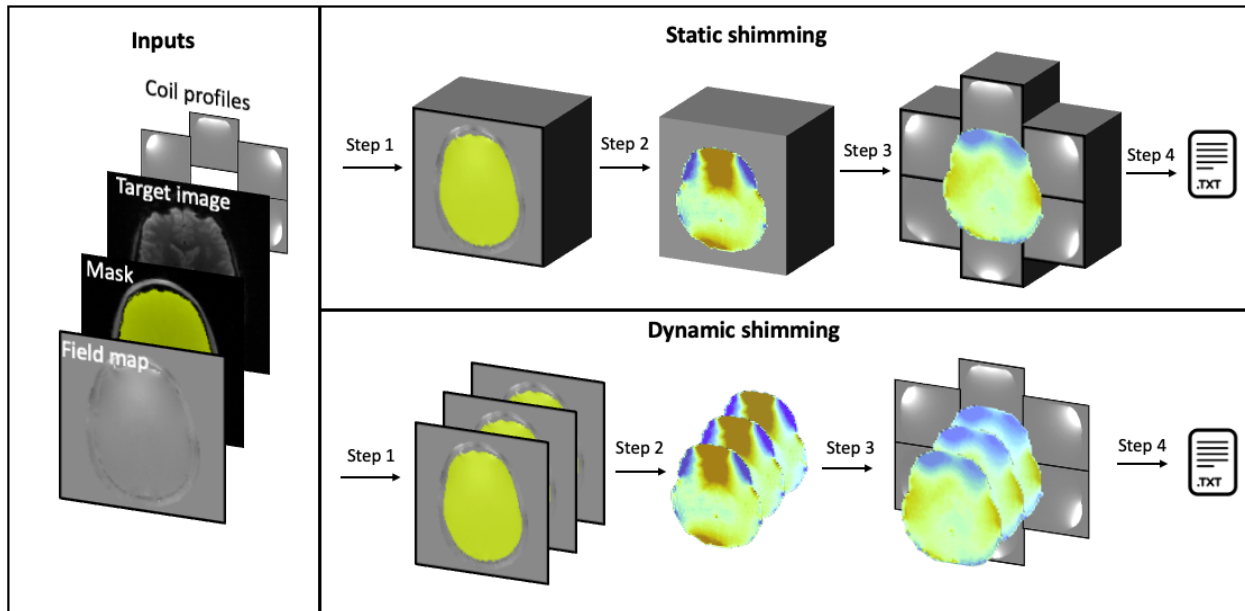


Figure 4.3: Overview of B0 static and dynamic shimming. **Step 1:** The mask is either considered as a single block (static) or multiple slice groups (dynamic), and resampled to the ΔB_0 field map space. **Step 2:** The ROI of the field map is extracted using the mask. **Step 3:** The coil profiles are resampled to the field map space and shimming coefficients are calculated based on the selected solver and criteria. **Step 4:** The coefficients are written to a text file.

4.4.1.5.3 Real-time dynamic shimming

In real-time shimming, the goal is to correct for both the static and time-varying parts of the magnetic field. Coefficients can be calculated globally or for each slice (dynamic). An implementation of real-time shimming was developed to correct for breathing-related time-varying magnetic fields. Multiple ΔB_0 field maps are acquired over time (e.g., while the participant is breathing), while an external signal is being recorded (e.g., chest motion via pressure readings from bellows). The inputs are (i) a 4D ΔB_0 field map, (ii) a 3D target image, (iii) a mask, (iv) coil profiles and (v) a probe that tracks breathing pattern (e.g., respiratory below). The more time points acquired in the 4D ΔB_0 field map will ensure a more robust fit at the expense of scan time. We have observed good results using 30 timepoints spanning more than 10 breathing cycles. The pressure probe should have a temporal resolution of at least the TR in gradient echo (GRE) acquisitions to update the pressure for each line of k-space.

The probe signal of pressure over time (t) is used alongside the field maps to extract the static and real-time component of the ΔB_0 field, for each voxel through a linear fit. The mask is then separated in slices and each slice is resampled on the field map. Two optimizations are then performed: (i) on the static component to find the static currents that best fit the static profile, and (ii) on the real-time component to find the coefficients that best fit the real-time profile. These yield $Coef_{static}$ and $Coef_{real-time}$ for each slice and each channel.

During shimming, the pressure (P) is read from the pressure probe at time of the RF pulse (t'). $Coef_{static}$ and $Coef_{real-time}$ of the slice being acquired for each coil channel are used to evaluate the following equation and calculate $Coef$ of each channel which will be applied for that read-out. $Coef$ scales linearly with pressure making sure that if the subject breathes more deeply than in the 4D field mapping sequence, a proper shim still takes place.

$$Coef = Coef_{static} + Coef_{real-time} \times P(t') \quad \text{Equation 4.1}$$

When using the scanner's gradient coil as shim coils, x, y and z gradients can be calculated from the pressure reading acquired at the time of the RF pulse (t'). Figure 4.4 shows a pulse sequence diagram of a custom multi-echo GRE sequence demonstrating how x, y and z gradients can be used with the described method to achieve real-time dynamic xyz-shimming.

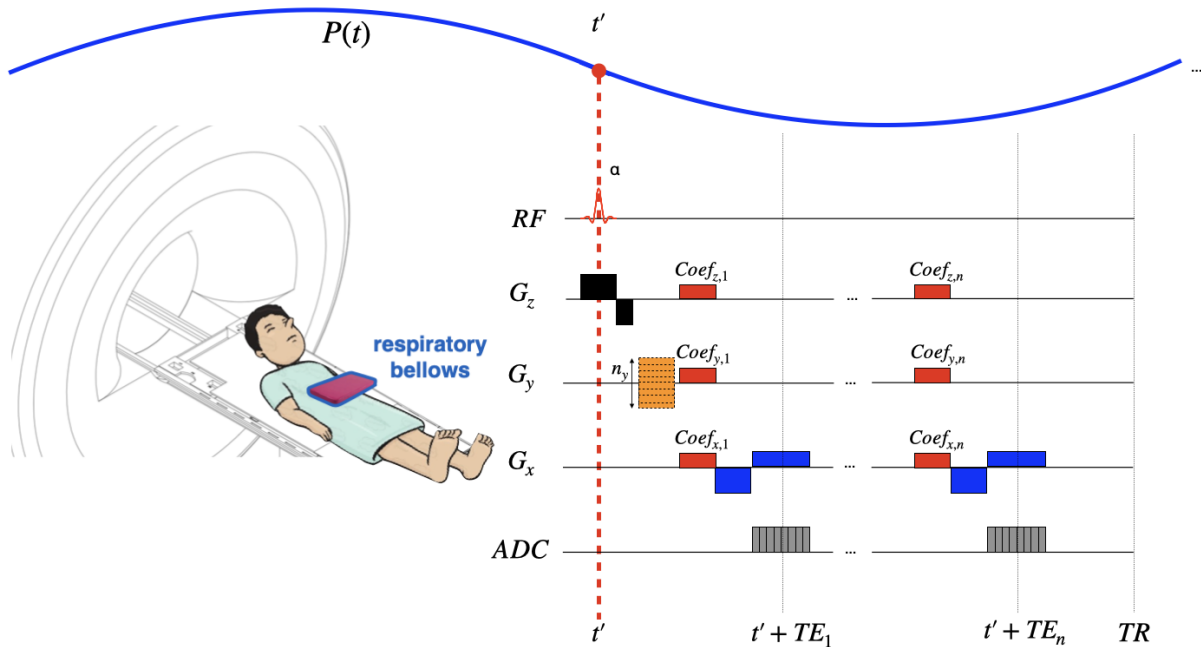


Figure 4.4: Real-time dynamic xyz-shimming sequence showing one line of k-space. Gradients (in red) along x, y and z are played out during the pulse sequence to correct for through slice and in-plane homogeneities. The amplitude of these gradients is modulated in real-time by the respiratory pressure trace. Note that the pressure reading was purposely made faster for illustration purpose (one TR is much faster than one breathing cycle).

4.4.1.6 B1 shimming

Performing B1 shimming using a multi-transmit coil requires prior knowledge of both the magnitude and phase of the B1 field generated by each transmit (Tx) element. From there, an optimization of the magnitude and phase values (shim weights) of the excitation waveforms sent to the different Tx elements can be performed to control the RF interferences and mitigate B1 inhomogeneities. To date, *Shimming toolbox* offers B1 static shimming, i.e., a single set of N_{Tx} shim weights (where N_{Tx} is the number of transmit elements) is optimized over the provided shimming ROI and is used over the whole imaging sequence.

To date, four different B1+ shimming algorithms fulfilling various needs are included in *Shimming Toolbox*:

- Reduction of the coefficient of variation: Minimizes the STD of the B1 magnitude divided by its mean, in order to homogenize it over the ROI. High B1 efficiencies are favored, with respect to safety guidelines.
- Targeting a specific B1 efficiency: The algorithm performs a magnitude least square optimization to target a B1 efficiency provided by the user. The B1 efficiency corresponds to the measured B1 (in μT) scaled by the reference excitation voltage applied at the scanner (in V). It is therefore expressed in T/V.
- Phase-only shimming: Only optimizes the phase of the excitation waveforms sent to the Tx elements. This optimization is fast and does not modify the power sent to the Tx system, but it results in a sub-optimal homogeneity compared to complex optimizations.
- Specific Absorption Rate efficiency: seeks to maximize the SAR efficiency, defined as the ratio of the mean B1 efficiency and the square root on the maximum local SAR value [65].

4.4.1.7 Outputs

Shimming coefficients are written in a text file that is intended to be read by a pulse sequence (e.g., for gradient coil-based dynamic shimming) and/or by the controller software of external shim coil amplifiers. The format of the text file can thus be customized to accommodate the required input style. Typical examples of output text files are shown in Figure 4.5. For B0 dynamic shimming using external AC/DC shim coils (Figure 4.5A), the text file lists the coefficients pertaining to each slice chronologically acquired when triggered by the TTL (transistor-transistor logic) pulse coming from the scanner. In this example, slices are acquired in an interleaved fashion. Each row is a different slice and each column is a different coil channel. For B0 real-time dynamic shimming based on the scanner's gradients (Figure 4.5B), the file format was adapted to be interpretable by the modified Siemens pulse sequence. Each block of three rows corresponds to a slice and within this block, specific coefficients correspond to the static coefficient, real-time coefficient and mean pressure measured from respiratory bellows. Figure 4.5C shows an output text file for a B1 static shimming experiment, wherein each row represents a transmit channel and the columns represent the magnitude and phase coefficients.

MRI scanners use different shimming coordinate systems depending on the manufacturer and on the method used to input the values. *Shimming Toolbox* can output the scanner coefficients in

different coordinate systems whether the goal is to manually input the values into the scanner or to automatically load them via a sequence.

For quality control, figures showing the field map before/after shimming (simulated) with the mask overlaid are also generated. Figures showing coil currents as well as useful metrics are also provided after an optimization.

A) B0 dynamic shimming				B) B0 real-time dynamic shimming				C) B1+ static shimming		
Slice	Ch 0	Ch 1	Ch2	corr_vec[type][slice]				Channel	mag	phase (°)
1	-0.047593,	0.335817,	-1.000000,	corr_vec[0][0]= 0.046519				Tx1	0.592	0.000
3	-0.168594,	1.000000,	-0.495496,	corr_vec[1][0]= -0.000001882504				Tx2	0.355	-120.189
5	-0.068879,	0.614811,	0.407032,	corr_vec[2][0]= 2322.067				Tx3	0.116	144.873
7	-0.069549,	0.999605,	1.000000,	corr_vec[0][1]= 0.046917				Tx4	0.482	141.369
9	0.017501,	0.893323,	1.000000,	corr_vec[1][1]= -0.000000150055				Tx5	0.574	20.498
11	0.069677,	0.669357,	-0.064084,	corr_vec[2][1]= 2322.067				Tx6	0.602	-138.222
13	0.121500,	0.414469,	-0.321574,	corr_vec[0][2]= 0.047192				Tx7	0.205	127.053
15	0.141564,	0.251979,	0.082040,	corr_vec[1][2]= 0.000000507478				Tx8	0.210	-7.456
17	0.138402,	0.169803,	0.119343,	corr_vec[2][2]= 2322.067						
0	0.090760,	0.127874,	0.143141,	corr_vec[0][3]= 0.047550						
2	0.049437,	0.063087,	0.185007,	corr_vec[1][3]= 0.000001342304						
4	0.060380,	0.068800,	0.052069,	corr_vec[2][3]= 2322.067						
6	0.109930,	0.047251,	-0.129722,	corr_vec[0][4]= 0.047769						
8	0.109704,	-0.004380,	-0.171574,	corr_vec[1][4]= 0.000002749780						
10	0.104192,	-0.033104,	-0.168877,	corr_vec[2][4]= 2322.067						
12	-0.091825,	-0.052284,	-0.066345,	corr_vec[0][5]= 0.047986						
14	-0.341657,	-0.057442,	0.079851,	corr_vec[1][5]= 0.000005209679						
16	-0.432324,	-0.060937,	0.053820,	corr_vec[2][5]= 2322.067						

Figure 4.5: Example text files output by *Shimming Toolbox*. **A)** Text file to be read by the pulse sequence during real-time dynamic shimming. Each block of three rows corresponds to a slice and within that block, a static coefficient, real-time coefficient and mean pressure is provided. **B)** Text file to be read by an Arduino Teensy board in the case of custom shim coils during dynamic shimming [52]. Each row corresponds to a slice and each column a coil channel. **C)** Text file with B1+ shimming coefficients where each row is a transmit channel and the columns are the magnitude and phase coefficients.

4.4.2 Imaging experiments

Here we present various ‘real world’ shimming experiments, performed across three imaging sites by three different users. All acquisitions followed proper ethics and were conducted with the approval of an institutional review board (IRB).

4.4.2.1 Scenario 1: B0 dynamic shimming using an AC/DC coil at 7 T

- What: B0 dynamic shimming
- Where: MGH Martinos Center for Biomedical Imaging, USA (7 T Siemens Terra)
- Coil: 31-channel custom AC/DC coil [46]
- Structure: Brain
- Sequence: GRE EPI

Shimming Toolbox was seamlessly installed on a laptop computer (MacBook Pro, M1 Max). The currents of the coil were set to 0 A and baseline acquisitions were acquired. An axial product dual-echo field mapping sequence was acquired to measure the B0 field with the following parameters: TR: 326 ms, TE: [2.04, 3.06] ms, FA: 20°, matrix: 112 × 112, in-plane resolution: 2 × 2 mm², slice thickness: 1.95 mm, 70 slices. Then an EPI was acquired slightly oblique to the field map to show the ability of *Shimming Toolbox* to use a field map and a target image with different orientations. The EPI had the following parameters: TR: 3180 ms, TE: 25 ms, FA: 80°, matrix: 174 × 174, in-plane resolution: 1.1 × 1.1 mm², slice thickness: 1 mm (150% gap), readout BW: 1512 Hz/pixel, echo spacing: 810 μs, effective echo spacing (GRAPPA R=4): 202.5 μs. Another EPI was acquired with the phase encoding direction reversed (AP and PA) to show image distortions related to the B0 field.

Shimming Toolbox converted the DICOM files into NIfTI files, calculated a field map, calculated a brain mask using BET [63] and calculated shimming coefficients for each slice and each channel of the 31-channel coil. A fat saturation pulse was used during the EPI; these can be problematic when using multi-coil (MC) arrays if the field produced outside the excited slice is within the bandwidth of the fat saturation pulse. To minimize artifacts, coefficients were added by *Shimming Toolbox* to set shim coefficients to zero during that pulse. These coefficients were written to a text file and sent to the microcontroller that controlled the shim amplifiers of the coil. The processing time from DICOM conversion to output text file was 4 minutes.

The same two EPI acquisitions (AP and PA) were then performed but this time the shim coil was active. Before the fat saturation pulse and each slice, a trigger connected to the shim coil driver was sent by the scanner to change the shim coefficients, allowing to acquire a dynamic shimmed EPI.

A field map was acquired in the same orientation as the EPI. The field map had the following parameters: TR: 280 ms, TE: [2.04, 3.06] ms, FA: 20°, matrix: 112 × 112, in-plane resolution: 2 × 2 mm², slice thickness: 2 mm (25% gap to match the EPI), 50 slices. The same shim coefficients as the EPI were used.

4.4.2.2 Scenario 2: Breathing-induced B0 real-time dynamic shimming at 3 T

- What: B0 real-time dynamic shimming
- Where: Neuroimaging Functional Unit, Centre de Recherche de l'Institut Universitaire de Gériatrie de Montréal, Canada (3 T Siemens Prisma-fit)
- Coil: Manufacturer's gradient coil (1st order for real-time dynamic-xyz) and 2nd order (for global static)
- Structure: Spinal cord
- Sequence: Custom GRE

A real-time shimming experiment was performed on the spinal cord of a healthy volunteer. The gradient coils current was updated in real-time (based on the breathing cycle) and following a dynamic fashion (ie: on a slice-by-slice basis), in order to correct both static and time-varying field homogeneities. Breathing-induced real-time dynamic z-shimming using this processing pipeline was introduced in a previous publication [10]. Briefly, respiratory bellows are attached to a patient to record their breathing pattern while a time series of B0 field maps are acquired. A linear fit of the pressure and calculated gradient maps allows to calculate a pressure related z-gradient to correct for through-slice inhomogeneities in real-time. In comparison with the previous publication, x and y gradients have been added here to also reduce in-plane field inhomogeneities.

Shimming Toolbox was installed on a laptop computer (MacBook Pro, Intel, 6 cores) and connected to the MRI console via ethernet to fetch the DICOMs as they were reconstructed. The standard volume-wise shimming using the 1st and 2nd order SH was performed on the scanner. A time series of 30 sagittal GRE two-echo field mapping sequence was acquired with the following parameters:

TR: 35 ms, TE: [2.14, 4.6] ms, FA: 20°, matrix: 88 × 128, partial Fourier: 7/8, in-plane resolution: 2.2 × 2.2 mm², slice thickness: 2.2 mm, 5 slices. Pressure bellows were placed on the subject's chest to measure the respiratory trace during the field map acquisition.

A modified GRE sequence capable of updating the scanner's 1st order xyz terms based on the respiratory trace was acquired. The standard shimming procedure was first run on the global volume using the scanners 1st and 2nd order shim coils. The following parameters were used: Axial orientation, TR: 189 ms, TE: [2.3, 4.5, 6.7, 8.9, 11.1, 13.3] ms, FA: 25°, matrix: 128 × 64, in-plane resolution: 2.34 × 2.34 mm², slice thickness: 3 mm, 12 slices.

Shimming Toolbox calculated the field maps and created a mask of the spinal cord automatically using SCT. For this particular experiment, the gradients along the x, y and z axis were calculated from the field maps. A linear fit of the pressure and gradient maps separated each map into a static and real-time component. The average per slice in the ROI was calculated for all components yielding shimming coefficients ($Coef_{xyz,static}$, $Coef_{xyz,real-time}$) which were written to a text file and automatically sent to the scanner console.

$$Coef_x = Coef_{x,static} + Coef_{x,real-time} \times P(t') \quad \text{Equation 4.2}$$

$$Coef_y = Coef_{y,static} + Coef_{y,real-time} \times P(t') \quad \text{Equation 4.3}$$

$$Coef_z = Coef_{z,static} + Coef_{z,real-time} \times P(t') \quad \text{Equation 4.4}$$

The same modified GRE sequence as described above was acquired, this time with real-time shimming activated. The sequence parameters and scanner global shimming coefficients were kept the same. The custom sequence read the x, y and z gradient coefficient corrections of the text file and appropriately adjusted the pulse sequence to correct for both static and real-time components of the magnetic field. Figure 4.4 shows the custom GRE pulse sequence used to apply the corrections.

4.4.2.3 Scenario 3: B1 static shimming at 7 T

- What: B1 static shimming
- Where: Brain Imaging Centre, Montreal Neurological Institute, Canada (7 T Siemens Terra)
- Coil: 8 Tx / 20 Rx channel custom DC coil [66]

- Structure: Spinal cord
- Sequence: Pre-saturated TurboFLASH B1 mapping

Before shimming, the individual B1 fields produced by each transmit element were measured using a pre-saturation turboFLASH B1 mapping technique [67]. This sequence is particularly fast, as it requires 64s to get individual sagittal B1 maps over a $240 \times 388 \times 84 \text{ mm}^3$ FOV with a $2 \times 2 \times 3.6 \text{ mm}^3$ resolution. As no abrupt variation of the B1 efficiency in the spinal-cord was observed on the B1 maps, this fairly low resolution was deemed sufficient to efficiently shim. For all experiments, the flip angle was set to 90° for the saturation pulse and 10° for the imaging pulse. The echo time was 1.79ms, the repetition time was 6.97 s, the bandwidth was 555 Hz/px, and the reference voltage was 400 V.

Anatomical images of the cervical and thoracic spine region were acquired using the MP2RAGE sequence [68]. As part of this MP2RAGE sequence, two GRE volumes (INV1 and INV2) with different inversion times ($TI_1=0.84 \text{ s}$, $TI_2=2.37 \text{ s}$) and flip angles ($FA_1=5^\circ$, $FA_2=6^\circ$) were acquired and used to compute a uniform T1-weighted image (UNI). After being exported offline, these anatomical images were used to perform an automated segmentation of the spinal cord using the SCT [64], so that it could be used as a ROI over which to shim. The anatomical images were also used to evaluate the homogeneity improvements after B1 shimming by re-running the MP2RAGE protocol and comparing the homogeneity in the spinal cord on UNI and GRE images before and after shimming.

The optimization of the complex shim weights (phase and magnitude of the pulses sent on the individual transmit elements) was performed using *Shimming Toolbox*. The optimization algorithm targeted a B1 efficiency of 15 nT/V in the ROI. The optimized shim weights were then manually input to the scanner so that they could be applied during the acquisition of the shimmed MP2RAGE sequence. This whole B1 shimming process took about 10 minutes and included B1 mapping, anatomical imaging, DICOM file exportation, spinal cord segmentation, shim weights optimization and manual input of the shim weights.

4.5 Results

4.5.1 Scenario 1: B₀ dynamic shimming using an AC/DC coil at 7 T

Figure 4.6 shows resulting field maps with the same slice orientation as the acquired target EPI acquisition. It shows a comparison between the field maps resulting from global shimming using up to the 2nd order spherical harmonics (*Global 2SH*), the predicted result from dynamic shimming the AC/DC coil (*Dynamic (predicted)*) and the acquired result after dynamic shimming with that coil (*Dynamic AC/DC*).

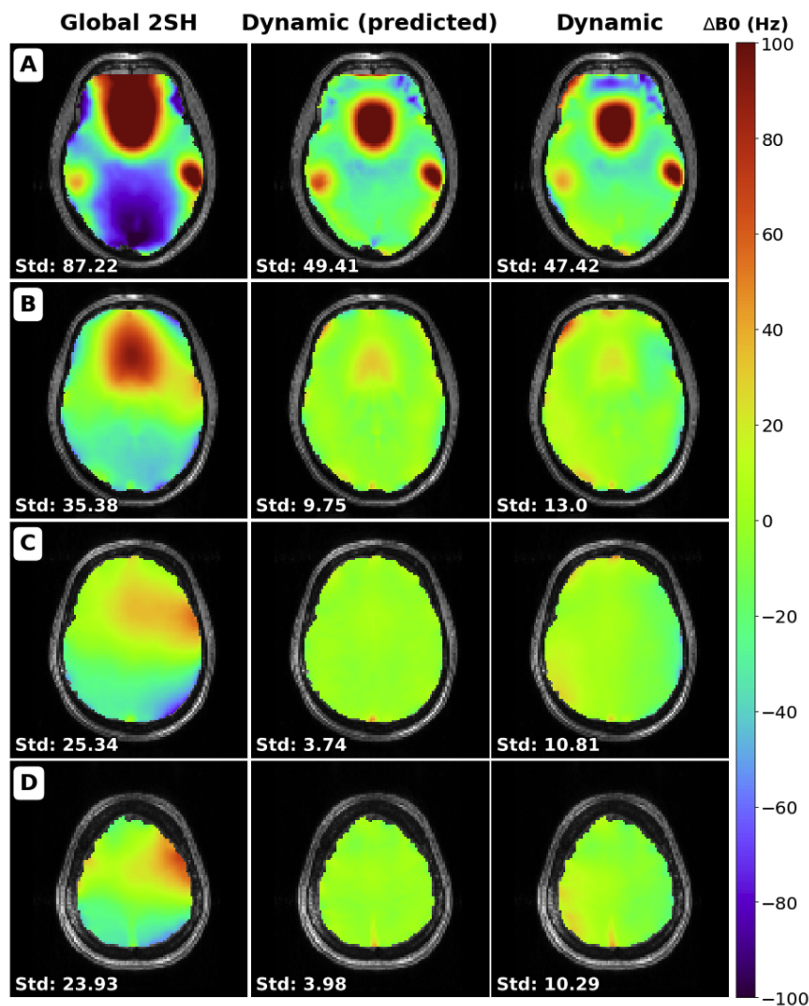


Figure 4.6: Comparison of field maps between the global 2nd order spherical harmonics on the whole brain, the predicted dynamic shim using the AC/DC custom coil and the acquired dynamic shim image with that coil. Standard deviation is shown for each slice in Hz. Slices numbers: A: 16, B: 24, C: 32, D: 40.

The dynamic shimming data are in agreement with the prediction, and show reduced inhomogeneity compared to the global shimming data. The STD of the B₀ field was computed in the whole brain, resulting in 73.80 Hz for global 2SH, 39.61 Hz for dynamic (predicted) and 39.15 Hz for dynamic shimming.

These results show an improvement of the STD between the global 2SH shimming and acquired dynamic shimmed field maps in the brain of 47.0%. A plot of the STD across slices is available in supporting Figure 4.7.

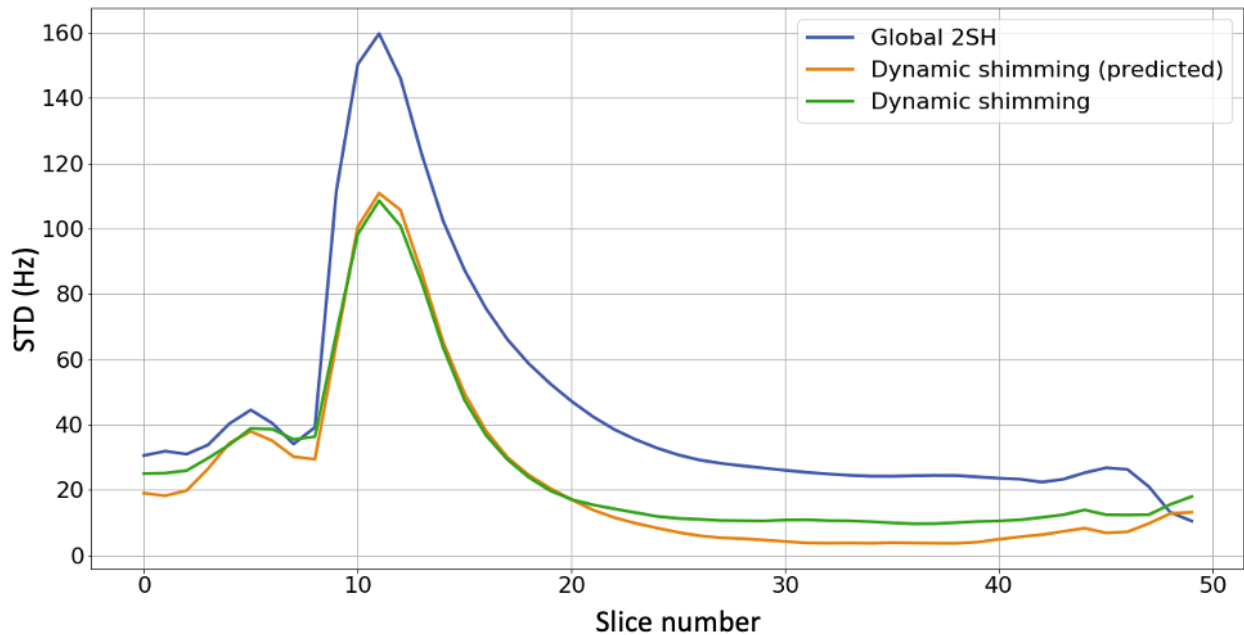


Figure 4.7: Comparison of the standard deviation of the B₀ field in the brain at 7T for each slice of acquired B₀ field maps between global 2nd order spherical harmonics shimming, predicted dynamic shimming and acquired dynamic shimming using an AC/DC coil.

Figure 4.8 shows EPI slices acquired on a healthy volunteer using global shimming up to the 2nd order spherical harmonics (Global 2SH) and using slice-optimized shimming with the 31-ch AC/DC shim coil (*Dynamic AC/DC*). Two opposite phase encoding directions are shown for each experiment to visualize the geometric distortions caused by the B₀ inhomogeneities (AP/PA). A brain mask outline in red was calculated using BET from an undistorted MPRAGE acquisition (MPRAGE reference). The outline is overlaid to help the comparison. Dynamic shimming showed improvements in geometric distortions when compared to global shimming. An animated GIF is included in supporting **Video S2** that more easily shows the distortions.

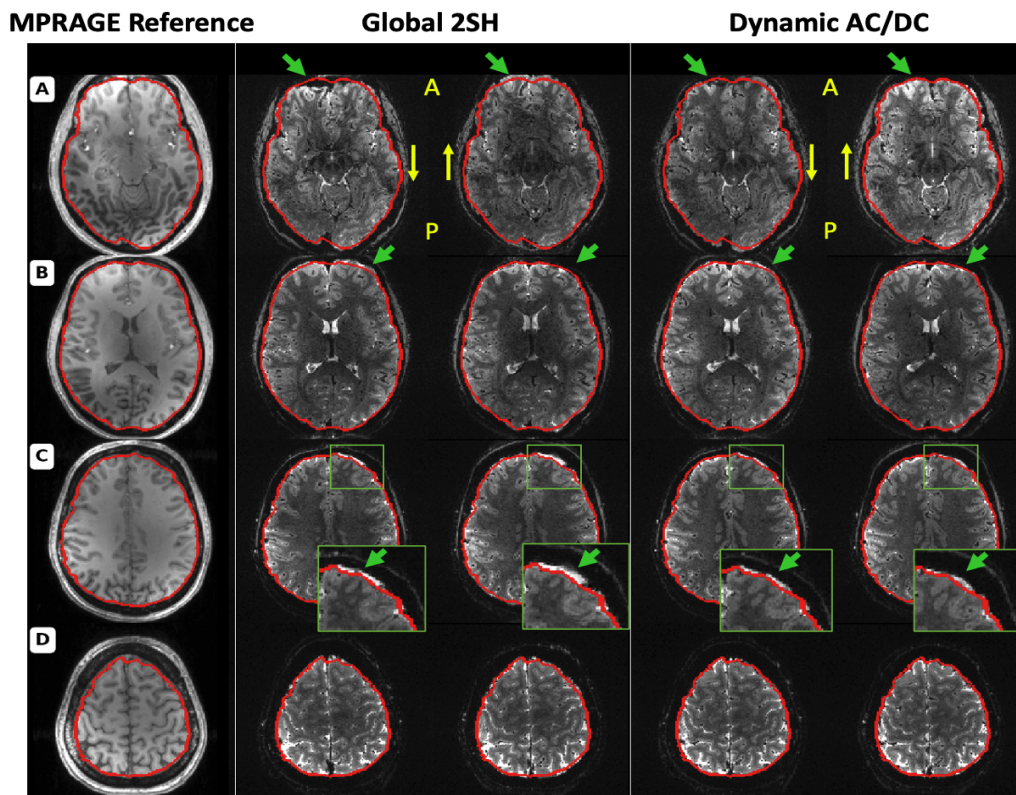


Figure 4.8: Comparison of the distortion between 2nd order SH global shimming and dynamic shimming using a 31-channel custom multi-coil shim array. Column 1 shows a reference MPRAGE acquisition where the brain outline was segmented for reference using BET and overlaid in red. Columns 2 through 5 show EPI acquisitions with the same acquisition parameters except for the shimming procedure and phase encoding direction. Columns 2 and 3 show global shimming using 2nd order spherical harmonics in the AP and PA phase encoding direction respectively. Column 4 and 5 show dynamic shimming using *Shimming Toolbox* and the multi-coil shim array with phase encoding direction of AP and PA respectively. Slices numbers: A: 16, B: 24, C: 32, D: 40.

4.5.2 Scenario 2: Breathing-induced B0 real-time dynamic shimming at 3 T

Figure 4.9 shows a comparison of the signal distribution within the spinal cord where the shimming ROI was defined between the 2nd order SH global shimming and real-time dynamic xyz-shimming. Average signal intensity across slices and echo times increased by 15.5% and STD decreased by 29.6%.

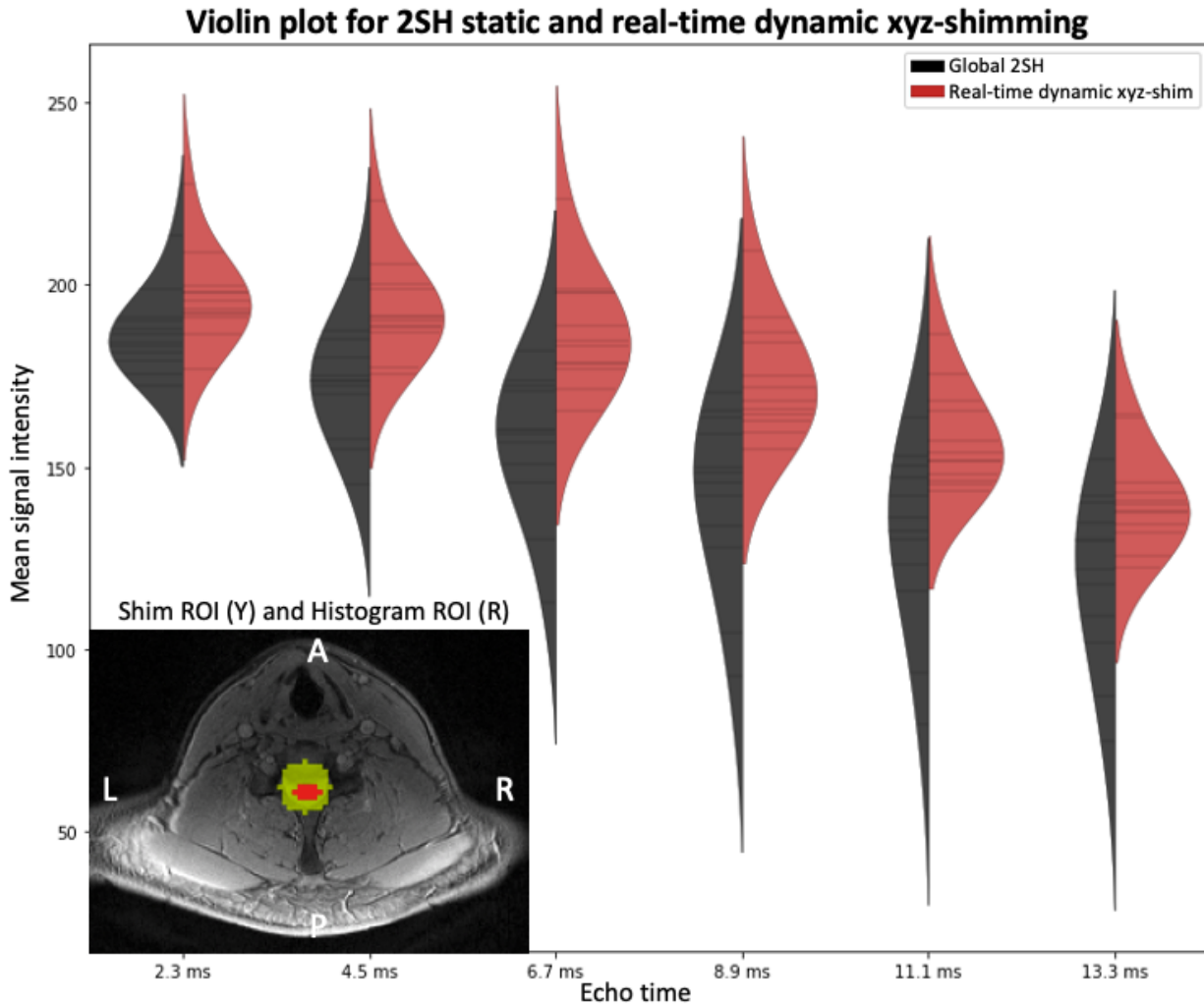


Figure 4.9: Violin plot comparing the signal distribution within the spinal cord with 2nd order global shimming (black) and with real-time dynamic xyz-shimming (red) for multiple echo times. Mean signal intensity across slices and echo times: global/real-time: 151.54/174.99. Average standard deviation within slices: global/real-time: 19.61/13.81. An axial slice showing the location of the shim ROI for real-time shimming as well as the segmented spinal cord is shown at the bottom left of the plot.

Figure 4.10 shows acquired axial 2nd order SH global shimmed (Global 2SH) and real-time dynamic xyz-shimmed images of the spinal cord. One can observe more contrast between the spinal cord and surrounding tissues as well as improved signal intensity.

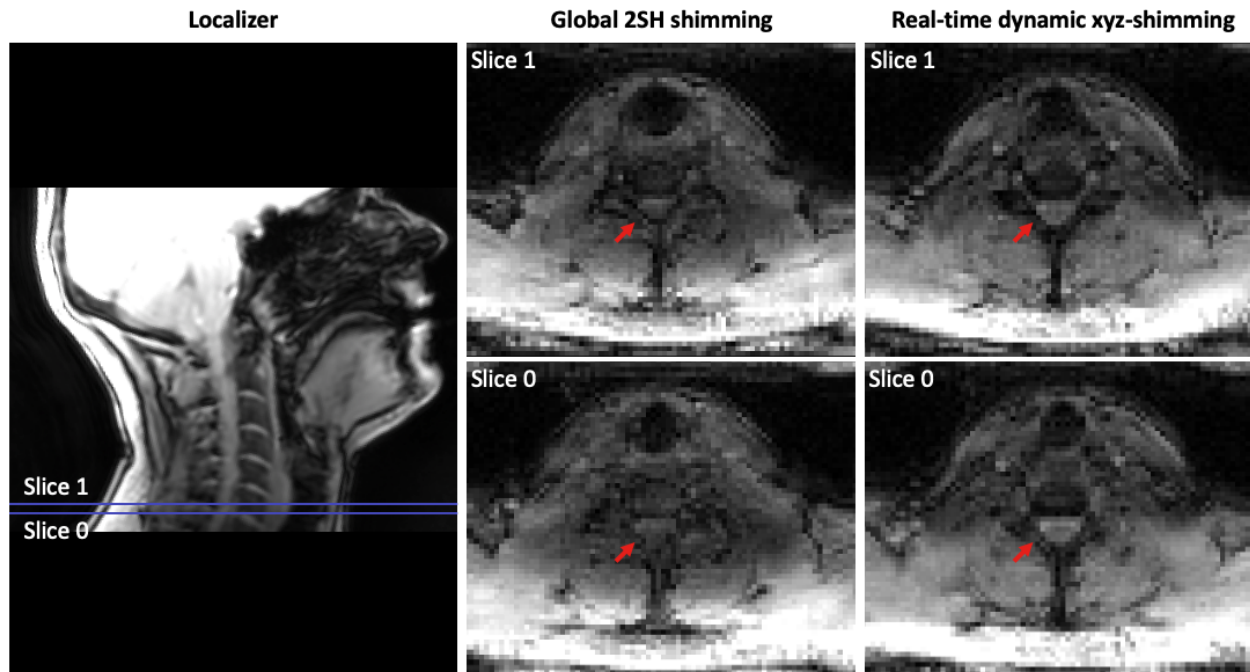


Figure 4.10: Comparison between 2nd order global shimming and real-time dynamic xyz-shimming in the spinal cord at 3 T. **(Left)** Localizer showing where the slices are located. **(Center and Right)** Slice number 1 and 2 of the same multi-echo GRE sequence acquired using 2nd order global shimming and real-time dynamic xyz-shimming.

4.5.3 Scenario 3: B1 static shimming at 7 T

Figure 4.11 presents the normalized intensity in the spinal cord on the MP2RAGE's UNI and GRE images, before and after B1 shimming. Spinal cords were automatically segmented on the circularly polarized (CP) mode and shimmed images. A co-registration was performed to make sure that the same anatomical regions were compared. After shimming the coefficient of variation in the spinal cord is reduced by 10.59% on UNI images (A, B) and 39.72% on INV2 GRE images (C, D). These results show that, when compared to the CP mode, which is the default excitation mode of the coil, the shim weights optimized by *Shimming Toolbox* effectively reduced the inhomogeneities in the ROI on anatomical images.

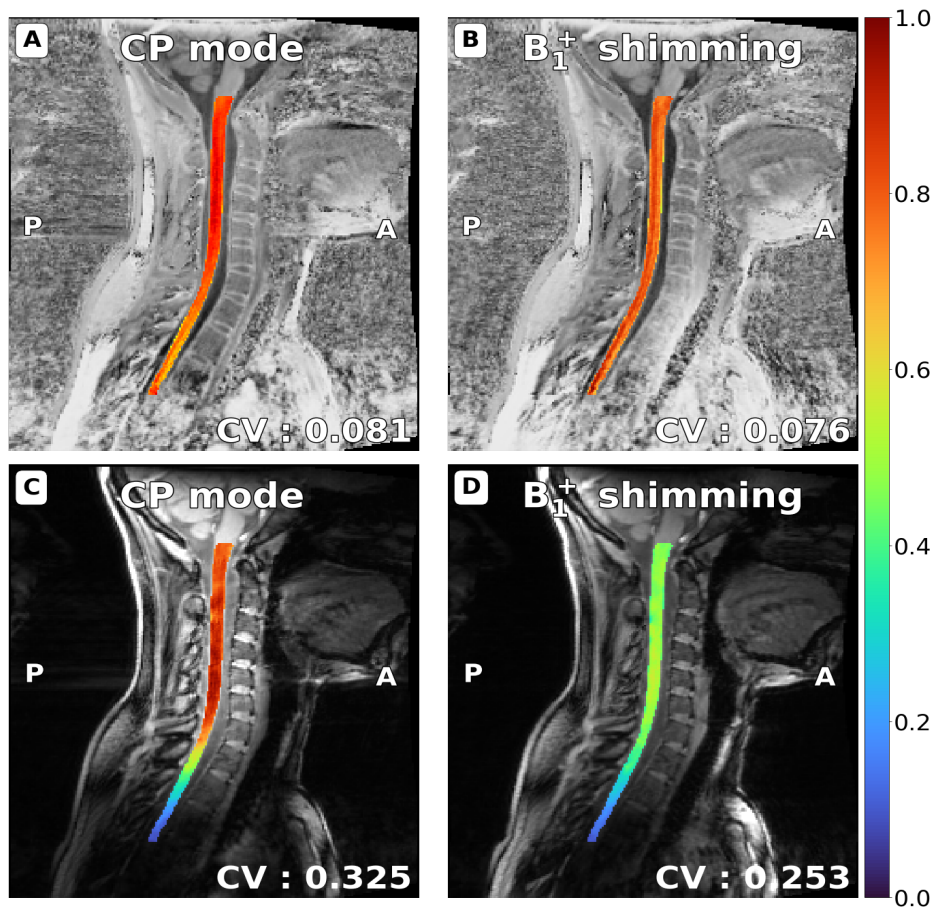


Figure 4.11: UNI (A, B) and GRE-INV2 images (C, D) spinal cord images from the MP2RAGE sequence, normalized by the maximum intensity in the spinal cord. Spinal cords were automatically segmented with SCT (and manually adjusted when required) on CP mode and shimmed images and a co-registration was performed. After shimming, the coefficient of variation in the spinal cord is reduced by 10.59% on UNI images (A, B) and 39.72% on GRE images (C, D).

4.6 Discussion

Shimming Toolbox is an end-to-end software package for prototyping new methods and performing B0 and B1 shimming experiments, including image format conversion, field mapping, coil calibration, masking and shimming. Below we discuss the results of the three trial experiments that were designed to validate *Shimming Toolbox*, as well as limitations and future improvements.

4.6.1 Validation experiments

The different scenarios have shown the versatility of *Shimming Toolbox* by homogenizing the B0 and the B1 fields. All scenarios were performed by different operators, at three different sites (3 T and 7 T) and using different sequences and applied to different anatomical parts.

The use of an AC/DC coil with dynamic shimming in the brain showed a reduction in the STD of the ΔB_0 field across slices. These results are consistent with the results obtained by this coil when it was first used and published [46]. Real-time dynamic xyz-shimming showed improvements in the STD and mean signal intensity in the spinal cord.

The results of the B1 shimming functionalities applied to the spinal cord were encouraging. To improve the B1 workflow efficiency, the pulse sequence could be modified to automatically read the B1 coefficients as a text file output by *Shimming Toolbox*, which would save ~ 2 minutes over the 10 minutes it took to perform the experiment. Similar to the B0 dynamic shimming feature demonstrated, dynamically updating B1 shimming on a slice-by-slice basis [16] is part of future developments. Thanks to the modularity of *Shimming Toolbox* (see further discussion below), the dynamic shimming optimization application programming interface (API) can easily be applied to the B1 shimming feature.

4.6.2 Modularity

Shimming Toolbox is built with modularity in mind. The different B0 techniques discussed in this work were implemented to be used in a variety of scenarios. *Shimming Toolbox* calculates coefficients appropriately for most static experiments and supports 2D acquisitions for dynamic shimming. This allows different sequences (EPI, GRE, spin echoes), different k-space trajectories (spiral, cartesian) and different experiments (fMRI, anatomical) to be used with global and dynamic shimming while real-time shimming requires a custom sequence.

The different APIs are built so that features can conveniently be added in the future. For example, adding 3rd party unwrapping algorithms can be done via a wrapper that can call the external software package executable. Shimming techniques can make use of the already developed APIs and shimming objective functions can be added with a few lines of code.

Shimming Toolbox has been designed to be used from the command line. This design decision allows *Shimming Toolbox* to be integrated into other software that can access the command line. *Shimming Toolbox* can also be implemented in other GUIs in the future (ITKsnap) which would allow users that rely on other viewers to stay in a more familiar environment. Similarly, if proprietary MR console environments and OS distros/versions allow it, *Shimming Toolbox* could be integrated directly on the scanner console so that scanning sessions are more efficient and more seamlessly integrated into existing scanning workflows.

4.6.3 Graphical User Interface (GUI) and scripts

The GUI can be used in scanning sessions to explore the data, find the right commands and the right parameters to execute. However, the GUI is inconvenient when speed is a priority. For better efficiency and to avoid user errors, a script can be written from the simple commands used in the GUI to automate the workflow of an imaging session. It also allows multi-subject experiments to be more convenient and straightforward. Using the same script for experiments performed at different sites allows the shimming process to be consistent across the different sessions. The script also outputs quality control figures allowing the user to make on the fly assessments on the quality of the shimming. Example scripts are available on the [Shimming Toolbox website](#).

4.6.4 Perspective

Other B₀ shimming features not currently implemented in *Shimming Toolbox* would be desirable. In the context of dynamic shimming, adding a regularization of the shimming coefficients across slices could alleviate the high switching rate constraints on the gradient and shim coils. About the optimizer module, other solvers (e.g., global minimum solvers, faster solvers) could offer better solutions for specific applications. Other shimming techniques that maximize signal intensity [69] could also be implemented.

The B₀ shimming pipeline relies on field maps for generating coil profiles and to generate the field to shim. By improving the field mapping pipeline, the coil profiles and field maps would be more

accurate which would in turn improve shimming. Field mapping algorithms using multiple echoes could improve the reliability of those field maps. Other phase unwrappers such as UMPIRE [34] and ROMEO [33] could provide more options if an unwrapper struggles with specific field maps.

Regarding B1 shimming features, beyond workflow improvements (for example, the text file with B1 magnitude/phase shimming coefficients file being read by a sequence) and the dynamic shimming feature mentioned earlier, we would like to make *Shimming Toolbox* compatible with additional B1 mapping methods that could be better suited to specific anatomical regions (e.g., by minimizing breathing induced artifacts [70]).

This article focuses on imaging applications, however B0 and B1 shimming is also crucial for spectroscopy applications. Future work should include validation of *Shimming Toolbox* for MR spectroscopy.

Shimming Toolbox aims at supporting all the popular MRI manufacturers. Support for Siemens systems is officially available and validated. Compatibility with other platforms (e.g., Philips, GE) will require slight modifications on the DICOM to BIDS conversion (ensuring that B0 and B1 mapping sequences are properly identified as such) and on the output text file. These developments are currently underway. If using external shim coils which do not interact with the MRI's proprietary software, *Shimming Toolbox* is *de facto* compatible regardless of the MRI manufacturer.

4.6.5 Open-source software development

Shimming Toolbox's goal is to provide shimming enthusiasts with an open, modular and transparent platform. We encourage the community to contribute to this open-source software. By centralizing, standardizing and making available state-of-the-art shimming techniques, researchers will have the necessary tools to conveniently perform MR experiments, compare coils, prototype new shimming techniques and reproduce experiments published by other groups.

4.7 Conclusion

Shimming Toolbox is an open-source software package for prototyping new methods and performing B0 and B1 shimming experiments. It was validated in various shimming experiments across field strengths, imaging sites and anatomy parts. We hope that *Shimming Toolbox* will

provide a platform on which the MRI community can collaborate, use state-of-the-art shimming techniques, contribute to new shimming techniques and make shimming research more transparent and reproducible.

4.8 Acknowledgements

We would like to thank all of the hard work from the many people that have worked on this project. A special thanks to Ryan Topfer, Ainsley Hill, Nick Guenther, Alexandru Foias, Joshua Newton, Lincoln Craven-Brightman, Johanan Idicula and Mathieu Boudreau. Funded by the Canada Research Chair in Quantitative Magnetic Resonance Imaging [950-230815], the Canadian Institute of Health Research [CIHR FDN-143263], the Canada Foundation for Innovation [32454, 34824], the Fonds de Recherche du Québec - Santé [322736], the Natural Sciences and Engineering Research Council of Canada [RGPIN-2019-07244], the Canada First Research Excellence Fund (IVADO and TransMedTech), the Courtois NeuroMod project, the Quebec BioImaging Network [5886, 35450], INSPIRED (Spinal Research, UK; Wings for Life, Austria; Craig H. Neilsen Foundation, USA), Mila - Tech Transfer Funding Program; NIH NIBIB U24 EB028984.

CHAPTER 5 GENERAL DISCUSSION

This chapter reviews the specific objectives of the research project and discusses the limitations linked to the project.

5.1 Develop *Shimming Toolbox*

As described in Chapter 4, a shimming software package called *Shimming Toolbox* was developed from the ground up to perform, prototype, and test B0 shimming experiments. The software provides the necessary tools to perform static shimming, dynamic shimming as well as real-time shimming experiments using both spherical harmonics and custom coil profiles. Those tools include image conversion, field map processing, mask creation, and different shimming techniques using multiple optimization criteria.

The toolbox has been developed on a public repository on GitHub (<https://github.com/shimming-toolbox/shimming-toolbox>) so that its source code can be available to all researchers. It provides a platform on which the research community can collaborate by implementing new, state of the art shimming experiments and test other research groups solutions.

The tools are written in Python and the repository was built to follow the structure of a typical Python package. The different APIs have been implemented to be used from the Python interpreter and additional code was written to make them accessible on the command line through a command line interface (CLI). This allows the user to use *Shimming Toolbox* with simple commands on the command line and exposes the toolbox so that it can be used by other tools such as a GUI.

5.2 Develop a graphical user interface

A graphical user interface was developed to interface with *Shimming Toolbox*'s CLIs. The GUI provides an intuitive way to operate the toolbox as well as look through imaging data. As opposed to Figure 4.1 which shows the GUI in the FSLEyes window. The following figure shows the GUI developed with all the different pipelines described in Chapter 4. In this specific tab, the B0 dynamic shimming pipeline along with its input options is shown.

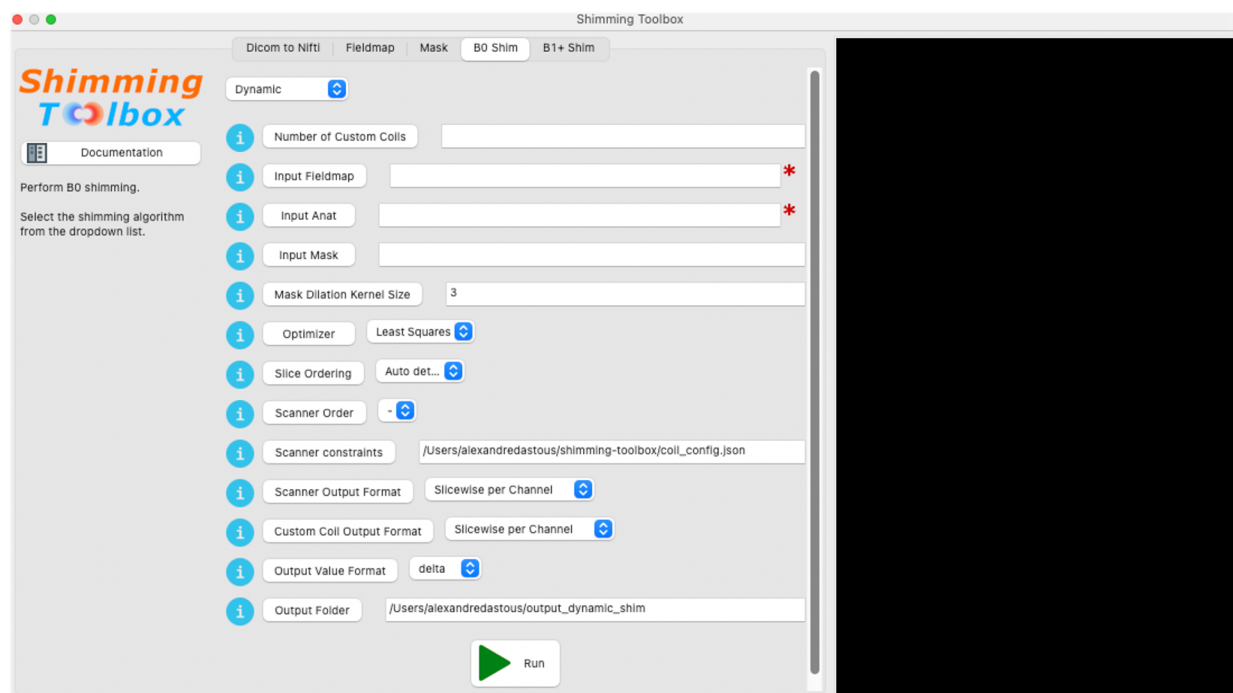


Figure 5.1: *Shimming Toolbox*'s GUI is shown with its different processing pipelines (Dicoms to Nifti, B0 field mapping, masking, B0 shimming and B1+ shimming) represented as tabs. In this tab, B0 dynamic shimming inputs and options can be seen.

5.3 Develop a website

As briefly described in Chapter 4, a website was built (<https://shimming-toolbox.org>) to provide users of *Shimming Toolbox* all the information they require to use it. Specifically, this includes installation instructions, tutorials, documentation about the different APIs and CLIs, information for developers and licensing information. The website's content is contained in the same GitHub repository as *Shimming Toolbox* and is processed and hosted online by Read the Docs.

5.4 Demonstrate *Shimming Toolbox*'s B0 shimming feasibility in different scenarios *in-vivo*

Two different B0 shimming experiments were performed to show *Shimming Toolbox*'s ability to shim in a variety of scenarios. It was used in a dynamic shimming scenario using a multi-coil on a 7 T scanner on the brain where the standard deviation of the B0 field improved. This resulted in a reduction of distortions in EPI images. A real-time dynamic xyz-shimming experiment was also

performed on a 3 T scanner on the spinal cord using the gradient coils (1st order SH). This experiment showed signal recovery in the spinal cord.

The development of *Shimming Toolbox* has allowed to develop a novel shimming approach which is real-time dynamic xyz-shimming [71]. Although not the focus of this work, it is one of *Shimming Toolbox*'s goal to enable developments such as this new technique.

5.5 B1+ shimming

One of the goals of *Shimming Toolbox* is to provide a versatile approach to shimming. This has allowed B1+ shimming to be seamlessly integrated in the software ecosystem. B1+ shimming uses much of the code developed as a result of developing for B0 shimming (e.g., image conversion, masking and others), follows a similar processing pipeline and reuses the tools used to deliver a satisfying user experience (e.g., simple installation process, a visual GUI, website and others). Similarly to B0 shimming, it is both Gaspard Cereza and my hope that *Shimming Toolbox* will help the B1 shimming community develop new B1 shimming research.

5.6 Limitations

One of the limitations presented in this work is that only one subject was tested for dynamic shimming. Although this validates the implementation of *Shimming Toolbox*, more experiments need to be done to accurately quantify the implemented techniques.

MRI experiments need to be fast since individuals can usually not stay in the scanner for a long time (i.e., more than one hour). Comfort and time restrictions create a need to be fast and efficient while acquiring images. Although this was considered while creating *Shimming Toolbox*, the software still takes valuable time to convert images, process field maps and calculate shimming coefficients. Depending on the acquisition and processing computer, it can take from a couple of seconds to multiple minutes for a user to complete the whole pipeline. This takes valuable time from an imaging session.

Shimming Toolbox has been tested and used on Siemens scanners. More precisely, the SH expansions, the output coefficient coordinate systems and necessary image metadata have been validated to work on Siemens scanners. *Shimming Toolbox* aims at being vendor agnostic but possible problems could be encountered if using Philips, GE or other vendor scanners.

The toolbox relies on field maps to know the field to correct as well as to characterize the field produced by coils. *Shimming Toolbox* currently only supports 2 echo field mapping techniques. These techniques fall short in images where lots of wraps and phase accumulation are present which could render the field map less accurate.

When using dynamic shimming, the switching of shimming coefficients that vary a lot between each slice can cause banding artifacts (varying bands of signal intensity) that are visible in the through slice direction, which can create geometric distortions. Although these effects were mitigated by penalizing multiple high coefficients as well as including multiple slices in the optimization process, some banding is still possible with coil constraints that allow high currents.

CHAPTER 6 CONCLUSION AND RECOMMENDATIONS

This project has successfully implemented an end-to-end shimming platform to perform B0 shimming experiments. A GUI and website were also developed to facilitate its use. *Shimming Toolbox* was successfully tested on dynamic shimming as well as on real-time dynamic xyz-shimming. The toolbox allows researchers to perform shimming experiments with a few minutes of additional scan time in a simple user interface. It is my hope that this tool will be used by the shimming community to further improve shimming research and make it more transparent and reproducible.

Multiple options are available for future development that could follow this work. *Shimming Toolbox*'s software could be optimized to require less time to compute shimming coefficients. This would allow users to do more experiments during single scanning sessions or simply reduce scan time. Another avenue would be to test and validate *Shimming Toolbox* on manufacturers other than Siemens (Philips and GE) so that most of the research community can use the software.

Implementation of different solvers and optimization criteria could make the toolbox a more complete tool. To improve the through slice inhomogeneities, regularization across slices could be implemented when doing dynamic shimming. Field mapping techniques using multiple echoes could improve the field map accuracy, which would make the shimming coefficients more accurate.

Another avenue for future developments would be to implement the toolbox directly on the scanner as this would allow a user to make the installation less cumbersome, speed the shimming process and improve the processing pipeline.

Regarding specific techniques, a logical continuation of the real-time dynamic xyz-shimming technique would be to make use of other shim coils like the 2nd order SH and custom coils. Other shimming techniques could be implemented such as techniques that maximize signal intensity [69] in EPI sequences.

REFERENCES

- [1] M. I. Karamat, S. Darvish-Molla, and A. Santos-Diaz, "Opportunities and challenges of 7 Tesla magnetic resonance imaging: A review," *Crit. Rev. Biomed. Eng.*, vol. 44, no. 1–02, pp. 73–89, 2016.
- [2] P. Jezzard and R. S. Balaban, "Correction for geometric distortion in echo planar images from B0 field variations," *Magn. Reson. Med.*, vol. 34, no. 1, pp. 65–73, Jul. 1995.
- [3] Y. Anzai, R. B. Lufkin, B. A. Jabour, and W. N. Hanafee, "Fat-suppression failure artifacts simulating pathology on frequency-selective fat-suppression MR images of the head and neck," *AJNR Am. J. Neuroradiol.*, vol. 13, no. 3, pp. 879–884, May 1992.
- [4] P. van Gelderen, J. A. de Zwart, P. Starewicz, R. S. Hinks, and J. H. Duyn, "Real-time shimming to compensate for respiration-induced B0 fluctuations," *Magn. Reson. Med.*, vol. 57, pp. 362–368, 2007.
- [5] J. Finsterbusch, "B0 Inhomogeneity and Shimming," in *Quantitative MRI of the Spinal Cord*, Elsevier, 2014, pp. 68–90.
- [6] A. M. Blamire, D. L. Rothman, and T. Nixon, "Dynamic shim updating: a new approach towards optimized whole brain shimming," *Magn. Reson. Med.*, vol. 36, no. 1, pp. 159–165, Jul. 1996.
- [7] K. M. Koch, S. McIntyre, T. W. Nixon, D. L. Rothman, and R. A. de Graaf, "Dynamic shim updating on the human brain," *J. Magn. Reson.*, vol. 180, no. 2, pp. 286–296, 2006.
- [8] J. Finsterbusch, F. Eippert, and C. Büchel, "Single, slice-specific z-shim gradient pulses improve T2*-weighted imaging of the spinal cord," *Neuroimage*, vol. 59, no. 3, pp. 2307–2315, Feb. 2012.
- [9] J. P. Stockmann and L. L. Wald, "In vivo B0 field shimming methods for MRI at 7T," *Neuroimage*, vol. 168, pp. 71–87, Mar. 2018.
- [10] E. Alonso-Ortiz, C. Tous, R. Topfer, and J. Cohen-Adad, "Real-Time Z-Shimming for Magnetic Resonance Imaging of the Spinal Cord," in *Proceedings of the 28th Annual Meeting of ISMRM, Sydney, Australia*, 2020.
- [11] C. Juchem, T. W. Nixon, S. McIntyre, D. L. Rothman, and R. A. de Graaf, "Magnetic field homogenization of the human prefrontal cortex with a set of localized electrical coils," *Magn. Reson. Med.*, vol. 63, no. 1, pp. 171–180, Jan. 2010.
- [12] J. P. Stockmann *et al.*, "A 32-channel combined RF and B0 shim array for 3T brain imaging," *Magn. Reson. Med.*, vol. 75, no. 1, pp. 441–451, Jan. 2016.
- [13] T. S. Ibrahim, R. Lee, A. M. Abduljalil, B. A. Baertlein, and P.-M. L. Robitaille, "Dielectric resonances and B1 field inhomogeneity in UHFMRI: computational analysis and experimental findings," *Magn. Reson. Imaging*, vol. 19, no. 2, pp. 219–226, Feb. 2001.
- [14] C. M. Collins, W. Liu, W. Schreiber, Q. X. Yang, and M. B. Smith, "Central brightening due to constructive interference with, without, and despite dielectric resonance," *J. Magn. Reson. Imaging*, vol. 21, no. 2, pp. 192–196, Feb. 2005.
- [15] G. J. Metzger, C. Snyder, C. Akgun, T. Vaughan, K. Ugurbil, and P.-F. Van de Moortele, "Local B1+ shimming for prostate imaging with transceiver arrays at 7T based on subject-dependent transmit phase measurements," *Magn. Reson. Med.*, vol. 59, no. 2, pp. 396–409, Feb. 2008.
- [16] A. T. Curtis, K. M. Gilbert, L. M. Klassen, J. S. Gati, and R. S. Menon, "Slice-by-slice B1+ shimming at 7 T," *Magn. Reson. Med.*, vol. 68, no. 4, pp. 1109–1116, Oct. 2012.

- [17] A. Paez, C. Gu, and Z. Cao, “Robust RF shimming and small-tip-angle multispoke pulse design with finite-difference regularization,” *Magn. Reson. Med.*, vol. 86, no. 3, pp. 1472–1481, Sep. 2021.
- [18] G. Cereza, “Development of an innovative solution minimizing RF field inhomogeneity and energy deposition in ultra-high field MRI applications,” MSc, École Polytechnique de Montréal, Montréal, Qc, 2022.
- [19] I. I. Rabi, J. R. Zacharias, S. Millman, and P. Kusch, “A new method of measuring nuclear magnetic moment,” *Phys. Rev.*, vol. 53, no. 4, pp. 318–318, Feb. 1938.
- [20] R. Damadian, “Tumor detection by nuclear magnetic resonance,” *Science*, vol. 171, no. 3976, pp. 1151–1153, Mar. 1971.
- [21] “The history, development and impact of computed imaging in neurological diagnosis and neurosurgery: CT, MRI, and DTI,” *Internet j. neurosurg.*, vol. 7, no. 1, 2010.
- [22] K. E. Keenan *et al.*, “Recommendations towards standards for quantitative MRI (qMRI) and outstanding needs,” *J. Magn. Reson. Imaging*, vol. 49, no. 7, pp. e26–e39, Jun. 2019.
- [23] W. R. Nitz and P. Reimer, “Contrast mechanisms in MR imaging,” *Eur. Radiol.*, vol. 9, no. 6, pp. 1032–1046, 1999.
- [24] J. Cohen-Adad, “GBM8378 - Principes d’imagerie biomédicale.” [Online]. Available: <https://moodle.polymtl.ca/course/view.php?id=134>.
- [25] M. Barth, F. Breuer, P. J. Koopmans, D. G. Norris, and B. A. Poser, “Simultaneous multislice (SMS) imaging techniques,” *Magn. Reson. Med.*, vol. 75, no. 1, pp. 63–81, Jan. 2016.
- [26] O. Speck, M. Weigel, and K. Scheffler, “Contrasts, mechanisms and sequences,” in *High-Field MR Imaging*, Berlin, Heidelberg: Springer Berlin Heidelberg, 2012, pp. 81–125.
- [27] C. Juchem and R. A. de Graaf, “B 0 magnetic field homogeneity and shimming for in vivo magnetic resonance spectroscopy,” *Anal. Biochem.*, vol. 529, pp. 17–29, Jul. 2017.
- [28] J. F. Schenck, “The role of magnetic susceptibility in magnetic resonance imaging: MRI magnetic compatibility of the first and second kinds,” *Med. Phys.*, vol. 23, no. 6, pp. 815–850, Jun. 1996.
- [29] A. D. Elster, “Sellar susceptibility artifacts: theory and implications,” *AJNR Am. J. Neuroradiol.*, vol. 14, no. 1, pp. 129–136, Jan. 1993.
- [30] M. E. Ladd *et al.*, “Pros and cons of ultra-high-field MRI/MRS for human application,” *Prog. Nucl. Magn. Reson. Spectrosc.*, vol. 109, pp. 1–50, Dec. 2018.
- [31] M. Jenkinson, “Fast, automated, N-dimensional phase-unwrapping algorithm,” *Magn. Reson. Med.* vol. 49, no. 1, pp. 193–197, 2003.
- [32] A. Karsa and K. Shmueli, “SEGUE: A Speedy rEgion-Growing Algorithm for Unwrapping Estimated Phase,” *IEEE Trans. Med. Imaging*, vol. 38, no. 6, pp. 1347–1357, Jun. 2019.
- [33] B. Dymerska *et al.*, “Phase unwrapping with a rapid opensource minimum spanning tree algorithm (ROMEO),” *Magn. Reson. Med.*, vol. 85, no. 4, pp. 2294–2308, Apr. 2021.
- [34] S. Robinson, H. Schödl, and S. Trattnig, “A method for unwrapping highly wrapped multi-echo phase images at very high field: UMPIRE,” *Magn. Reson. Med.*, vol. 72, no. 1, pp. 80–92, Jul. 2014.
- [35] S. Robinson and J. Jovicich, “B0 mapping with multi-channel RF coils at high field,” *Magn. Reson. Med.*, vol. 66, no. 4, pp. 976–988, Oct. 2011.
- [36] A. D. Elster, “QUESTIONS AND ANSWERS IN MRI,” *mriquestions*. [Online]. Available: <https://mriquestions.com>.
- [37] J. W. Pan, K.-M. Lo, and H. P. Hetherington, “Role of very high order and degree B0 shimming for spectroscopic imaging of the human brain at 7 tesla,” *Magn. Reson. Med.*, vol. 68, no. 4, pp. 1007–1017, Oct. 2012.

- [38] C. Juchem, T. W. Nixon, S. McIntyre, D. L. Rothman, and R. A. de Graaf, "Magnetic field modeling with a set of individual localized coils," *J. Magn. Reson.*, vol. 204, no. 2, pp. 281–289, Jun. 2010.
- [39] R. Topfer *et al.*, "A 24-channel shim array for the human spinal cord: Design, evaluation, and application," *Magn. Reson. Med.*, vol. 76, no. 5, pp. 1604–1611, 2016.
- [40] H. Han, A. W. Song, and T.-K. Truong, "Integrated parallel reception, excitation, and shimming (iPRES)," *Magn. Reson. Med.*, vol. 70, no. 1, pp. 241–247, Jul. 2013.
- [41] M. Schwerter *et al.*, "Interslice current change constrained B0 shim optimization for accurate high-order dynamic shim updating with strongly reduced eddy currents," *Magn. Reson. Med.*, vol. 82, no. 1, pp. 263–275, Jul. 2019.
- [42] C. Juchem, T. W. Nixon, P. Diduch, D. L. Rothman, P. Starewicz, and R. A. de Graaf, "Dynamic shimming of the human brain at 7 Tesla," *Concepts Magn. Reson. Part B Magn. Reson. Eng.*, vol. 37B, no. 3, pp. 116–128, Jul. 2010.
- [43] J. Finsterbusch, C. Sprenger, and C. Büchel, "Combined T2*-weighted measurements of the human brain and cervical spinal cord with a dynamic shim update," *Neuroimage*, vol. 79, pp. 153–161, Oct. 2013.
- [44] C. Juchem, T. W. Nixon, S. McIntyre, V. O. Boer, D. L. Rothman, and R. A. de Graaf, "Dynamic multi-coil shimming of the human brain at 7 T," *J. Magn. Reson.*, vol. 212, no. 2, pp. 280–288, Oct. 2011.
- [45] C. Juchem, S. Umesh Rudrapatna, T. W. Nixon, and R. A. de Graaf, "Dynamic multi-coil technique (DYNAMITE) shimming for echo-planar imaging of the human brain at 7 Tesla," *Neuroimage*, vol. 105, pp. 462–472, Jan. 2015.
- [46] J. P. Stockmann *et al.*, "A 31-channel integrated 'AC/DC' B0 shim and radiofrequency receive array coil for improved 7T MRI," *Magn. Reson. Med.*, vol. 87, no. 2, pp. 1074–1092, Feb. 2022.
- [47] C. Juchem, "B0 Detoxification through Magnetic Field Shimming."
- [48] J.-F. Nielsen *et al.*, "An open toolbox for harmonized B0 shimming," presented at the *Proc. Intl. Soc. Mag. Reson. Med.*
- [49] T. S. Ibrahim, Y.-K. Hue, and L. Tang, "Understanding and manipulating the RF fields at high field MRI," *NMR Biomed.*, vol. 22, no. 9, pp. 927–936, Nov. 2009.
- [50] R. Topfer, A. Foias, N. Stikov, and J. Cohen-Adad, "Real-time correction of respiration-induced distortions in the human spinal cord using a 24-channel shim array," *Magn. Reson. Med.*, vol. 80, no. 3, pp. 935–946, Sep. 2018.
- [51] C. Juchem, T. W. Nixon, P. Diduch, D. L. Rothman, P. Starewicz, and R. A. De Graaf, "Dynamic shimming of the human brain at 7 T," *Concepts Magn. Reson. Part B Magn. Reson. Eng.*, vol. 37, no. 3, pp. 116–128, 2010.
- [52] J. P. Stockmann *et al.*, "An integrated 32ch RF-shim array coil for improved B0 shimming of the brain at 7 Tesla," in *Proc Intl Soc Magn Reson Med*, 2017, vol. 26, p. 0967.
- [53] F. O. Zelaya, W. U. Roffmann, S. Crozier, S. Teed, D. Gross, and D. M. Doddrell, "Direct visualisation of B1 inhomogeneity by flip angle dependency," *Magn. Reson. Imaging*, vol. 15, no. 4, pp. 497–504, 1997.
- [54] T. S. Ibrahim, R. Lee, A. M. Abduljalil, B. A. Baertlein, and P.-M. L. Robitaille, "Dielectric resonances and B1 field inhomogeneity in UHF MRI: computational analysis and experimental findings," 2001. [Online]. Available: [http://dx.doi.org/10.1016/S0730-725X\(01\)00300-9](http://dx.doi.org/10.1016/S0730-725X(01)00300-9). [Accessed: 10-Aug-2020].
- [55] Juchem, "B0DETOX-B0 detoxification software for magnetic field shimming," *Columbia TechVenture (CTV), License CUI7326*.

- [56] C. M. Deniz, R. Brown, R. Lattanzi, L. Alon, D. K. Sodickson, and Y. Zhu, “Maximum efficiency radiofrequency shimming: Theory and initial application for hip imaging at 7 tesla,” *Magn. Reson. Med.*, vol. 69, no. 5, pp. 1379–1388, May 2013.
- [57] A. Beqiri, *mriphysics/cardiac_RF_shimming: Added tracking by Zenodo*. 2017.
- [58] P. McCarthy, *FSLeves*. 2019.
- [59] X. Li, P. S. Morgan, J. Ashburner, J. Smith, and C. Rorden, “The first step for neuroimaging data analysis: DICOM to NIfTI conversion,” *J. Neurosci. Methods*, vol. 264, pp. 47–56, May 2016.
- [60] K. J. Gorgolewski *et al.*, “The brain imaging data structure, a format for organizing and describing outputs of neuroimaging experiments,” *Sci Data*, vol. 3, p. 160044, Jun. 2016.
- [61] A. Karakuzu *et al.*, “A joint-community effort to standardize quantitative MRI data: Updates from the BIDS extension proposal,” in *Proc. Intl. Soc. Mag. Reson. Med., Sydney, Australia*, 2020.
- [62] “Dcm2Bids.” [Online]. Available: <https://github.com/UNFmontreal/Dcm2Bids>.
- [63] S. M. Smith, “BET: Brain extraction tool,” *FMRIB TR00SMS2b*, Oxford Centre for Functional Magnetic Resonance Imaging of the Brain), Department of Clinical Neurology, Oxford University, John Radcliffe Hospital, Headington, UK, 2000.
- [64] B. De Leener *et al.*, “SCT: Spinal Cord Toolbox, an open-source software for processing spinal cord MRI data,” *Neuroimage*, Oct. 2016.
- [65] N. I. Avdievich *et al.*, “Evaluation of transmit efficiency and SAR for a tight fit transceiver human head phased array at 9.4 T,” *NMR Biomed.*, vol. 30, no. 2, Feb. 2017.
- [66] R. N. Lopez *et al.*, “Integrated AC/DC coil and dipole Tx array for 7T MRI of the spinal cord,” in *Proceedings of the 27th Annual Meeting of ISMRM, Montreal, Canada*, 2019.
- [67] S. Chung, D. Kim, E. Breton, and L. Axel, “Rapid B1+ mapping using a preconditioning RF pulse with TurboFLASH readout,” *Magn. Reson. Med.*, vol. 64, no. 2, pp. 439–446, Aug. 2010.
- [68] J. P. Marques, T. Kober, G. Krueger, W. van der Zwaag, P.-F. Van de Moortele, and R. Gruetter, “MP2RAGE, a self bias-field corrected sequence for improved segmentation and T1-mapping at high field,” *Neuroimage*, vol. 49, no. 2, pp. 1271–1281, Jan. 2010.
- [69] M. Kaptan *et al.*, “Automated slice-specific z-shimming for fMRI of the human spinal cord,” *bioRxiv*, p. 2021.07.27.454049, 28-Jul-2021.
- [70] S. Dietrich *et al.*, “3D Free-breathing multichannel absolute B 1 + Mapping in the human body at 7T,” *Magn. Reson. Med.*, vol. 85, no. 5, pp. 2552–2567, May 2021.
- [71] D. Papp, A. D’Astous, J. Cohen-Adad, and E. Alonso-Ortiz, “Realtime dynamic xyz-shimming in the cervical spinal cord,” in *Proc. Intl. Soc. Mag. Reson. Med.*, 2022.